



저작자표시-비영리-변경금지 2.0 대한민국

이용자는 아래의 조건을 따르는 경우에 한하여 자유롭게

- 이 저작물을 복제, 배포, 전송, 전시, 공연 및 방송할 수 있습니다.

다음과 같은 조건을 따라야 합니다:



저작자표시. 귀하는 원저작자를 표시하여야 합니다.



비영리. 귀하는 이 저작물을 영리 목적으로 이용할 수 없습니다.



변경금지. 귀하는 이 저작물을 개작, 변형 또는 가공할 수 없습니다.

- 귀하는, 이 저작물의 재이용이나 배포의 경우, 이 저작물에 적용된 이용허락조건을 명확하게 나타내어야 합니다.
- 저작권자로부터 별도의 허가를 받으면 이러한 조건들은 적용되지 않습니다.

저작권법에 따른 이용자의 권리는 위의 내용에 의하여 영향을 받지 않습니다.

이것은 [이용허락규약\(Legal Code\)](#)을 이해하기 쉽게 요약한 것입니다.

[Disclaimer](#)

Master's Thesis

Carbon-Supported Fe_2O_3 and TiO_2 Photoanodes for
Enhanced Photoelectrochemical Cell Performance

Ki-Yong Yoon

Department of Energy and Chemical engineering

Graduate School of UNIST

2015

Carbon-Supported Fe₂O₃ and TiO₂ Photoanodes for Enhanced Photoelectrochemical Cell Performance

Ki-Yong Yoon

Department of Energy and Chemical engineering

Graduate School of UNIST

Carbon-Supported Fe₂O₃ and TiO₂ Photoanodes for Enhanced Photoelectrochemical Cell Performance

A dissertation
submitted to the Graduate School of UNIST
in partial fulfillment of the
requirements for the degree of
Master of Science

Ki-Yong Yoon

7. 15. 2015

Approved by



Advisor

Ji-Hyun Jang

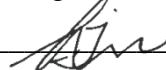
Carbon-Supported Fe₂O₃ and TiO₂ Photoanodes for Enhanced Photoelectrochemical Cell Performance

Ki-Yong Yoon

This certifies that the dissertation of Ki-Yong Yoon is approved.

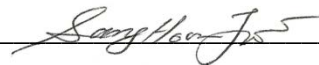
7. 15. 2015

signature




Advisor: Ji-Hyun Jang

signature



Sang Hoon Joo

signature



Kwanyong Seo

Abstract

Since the worldwide demands for energy is increasing, the consideration of environmental issues has been sharply required. Developing clean, low-cost and renewable fuel sources is a key challenge facing mankind in order to meet the energy and environment demands. Electrolysis of water is one of the methods of hydrogen generation. However, it is an energy intensive process. To produce clean energy, such as hydrogen, photoelectrochemical (PEC) cell is widely considered as one of most promising methods to split water when driven by abundant solar energy. We have focused photoanode materials, hematite and titanium dioxide, which is one of PEC components. In the hematite case, we have shown that by coupling graphene inverse opal structure with hematite, the problem of low diffusion length and low absorption in hematite was efficiently addressed, and thereby the water splitting photocurrent density generated by hematite could be greatly enhanced. This study can be readily extended to other metal oxide materials and systems, which provide strong potential for our strategy in energy conversion system. In the case of titanium dioxide, we made heterojunction with cadmium selenide (CdSe) for visible range absorption. However, CdSe quantum dot is often unstable in water under irradiation of light due to their relatively slower interfacial hole transfer kinetics as compared to their electron injection rates. To overcome this problem, we have successfully fabricated a novel graphene quantum dot supported CdSe-sensitized photoanode for visible-working PEC system. By modifying photoanode with graphene quantumdot, photocurrent density was retained almost unchanged for 300 minutes irradiation and the photocurrent density increased by 1.2 times relative to that without graphene quantum dot. Our work suggests a straightforward way to develop efficient and durable quantum-dot-sensitized photoanodes for PEC hydrogen generation.

Contents

Contents	3
Chapter 1. Introduction of Photo-electrochemical (PEC) Cell.	8
1.1 Hydrogen: fuel of the future.....	8
1.2 Hydrogen generation using solar energy.....	11
1.3 Reaction mechanism of photoelectrochemical cell.....	13
1.4 References	16
Chapter 2. Hematite-Based Photo-electrochemical cell Supported by Graphene Inverse Opal Structures	17
2.1. Introduction.....	17
2.2 Experimental and characterization.....	18
2.2.1 Preparation of Graphene Inverse Opal (GIO).....	18
2.2.2 Preparation of pristine to α -Fe ₂ O ₃ and to α -Fe ₂ O ₃ /GIO	18
2.2.3 Photo-electrochemical measurement	19
2.3 Results and Discussion.....	20
2.4 Conclusion.....	40
2.5 References	41
Chapter 3. Graphene Quantum-Dot Protected Cadmium Selenide Quantum-Dot Sensitized Photoanode for Efficient Photo-electrochemical Cells with Enhanced Stability and Performance.....	43
3.1 Introduction.....	43
3.2 Experimental Procedures	44
3.2.1 Synthesis of GQDs.....	44
3.2.2 Preparation of GQDs/CdSe/P25 photoanode.....	44
3.2.3 Photo-electrochemical measurement	45
3.3 Results and Discussion.....	46
3.4 Conclusion	67
3.5 References.....	68

List of Figures

Figure 1.1 Future prospects of hydrogen energy use

Figure 1.2 comparative emission of polluting gases (stated in carbon units per km) for vehicles motorized by today's internal combustion engine using gasoline energy compared to vehicles powered by fuel cells

Figure 1.3 Candidate materials for photoelectrode

Figure 1.4 The system of photoelectrochemical cell for water photoelectrolysis

Figure 2.1 Illustration for the fabrication of α -Fe₂O₃/GIO

Figure 2.2 SEM images of assembled PS opal (a,b) and NIO structure (c,d)

Figure 2.3 XRD analysis of α -Fe₂O₃/GIO with various annealing temperatures

Figure 2.4 SEM images of (a) GIO after etching nickel and (b) α -Fe₂O₃/GIO. (c-d) TEM images of α -Fe₂O₃/GIO. The inset images in (c) and (d) are SAED pattern and (110) lattice plane of α -Fe₂O₃, respectively

Figure 2.5 (a) Top view of SEM image and elemental mapping (b-d) for α -Fe₂O₃/GIO by SEM-EDX

Figure 2.6 BET analysis of (a) GIO and (b) α -Fe₂O₃/GIO

Figure 2.7 SEM images of β -FeOOH/GIO which show the variations in the size of NPs at various concentrations of FeCl₃·6H₂O solution. (a) 5mM, (b) 10mM, (c) 25mM and (d) 50 mM. The insets are the corresponding TEM images

Figure 2.8 (a) photocurrent behavior and (b) XRD analysis of the samples prepared by single step annealing at 750 °C (black line) and by two-step annealing at 350 °C for 4 hrs and 750 °C for 1hr (red line)

Figure 2.9 (a) XRD analysis of NIO (black line) and α -Fe₂O₃/GIO (red line) on FTO substrate. (b) Raman spectrum of GIO

Figure 2.10 Raman analysis of α -Fe₂O₃/GIO

Figure 2.11 Optical properties of α -Fe₂O₃/GIO. (a) Diffuse reflectance spectra. (b) UV-visible spectra

Figure 2.12 Tauc plot for α -Fe₂O₃ and α -Fe₂O₃/GIO

Figure 2.13 Photocurrent behaviors of α -Fe₂O₃/GIO. (a) The photocurrent vs. potential of α -Fe₂O₃ and α -Fe₂O₃/GIO under UV-visible and dark conditions. (b) I-t curve of α -Fe₂O₃/GIO at a bias of 1.5 V vs. RHE under UV-visible light illumination. (c) Nyquist plots and (d) IPCE of α -Fe₂O₃ and α -Fe₂O₃/GIO at a bias of 0.5 V vs. open circuit potential under illumination

Figure 2.14 Schematic diagram of water splitting of α -Fe₂O₃/GIO with photon trapping effects and direct contact of α -Fe₂O₃ with the 3D-graphene nano-network conductive electrode

Figure 3.1 Schematic illustration of (a) the proposed band diagram and (b) the fabrication procedure for GQDs/CdSe/P25. P25 (I), CdSe/P25 (II), and GQDs/CdSe/P25 (III)

Figure 3.2 UPS data for band gap alignment. (a) Full spectra of UPS for the valence band position and band energy of GQDs/CdSe/P25. (b) UPS for CdSe/P25 and (c) GQDs for valence band position. (d) The energy diagram

Figure 3.3 Characterization of GQDs: (a) UV-VIS absorption spectrum of GQDs. (b) Normalized PL spectra of the GQDs with different excitation wavelengths. (c) TEM and HR TEM images. (d) XPS spectra

Figure 3.4 (a) TEM images of GQDs/CdSe/P25. (b) Zoomed-up images of the highlighted region in (a). (c) Time-resolved PL decay profiles of CdSe/P25 and GQDs/CdSe/P25

Figure 3.5 XPS analysis of GQDs/CdSe/P25

Figure 3.6 (a) Raman spectra and (b) FT-IR spectrum

Figure 3.7 XRD analysis of GQDs/CdSe/P25

Figure 3.8 Photoluminescence (PL) spectra of GQDs and GQDs/CdSe/P25

Figure 3.10 (a) J-V curve and (b) EIS for GQDs/CdSe/P25 with different GQD dipping time of 1h, 2h, and 3h

Figure 3.11 Photocurrent responses of CdSe/P25 and GQDs/CdSe/P25 under UV-visible and visible (>420 nm) light illumination

Figure 3.12 The J-T curve of (a) CdSe/P25 and (b) GQDs/CdSe/P25 at a bias of 0.3 V under light-chopping conditions. (c) Schematic diagram of the photoexcited hole transfer process

Figure 3.9 (a) UV-VIS absorption spectra of the GQD, P25, CdSe/P25 and GQDs/CdSe/P25 photoanodes. (b) Linear sweep voltammetric (J-V) curves of the three kinds of photoanodes under simulated sunlight illumination. (c) Impedance spectroscopy of CdSe/P25 and GQDs/CdSe/P25. (d) A comparison of the IPCE spectra of the two photoanodes measured at 0.3 V vs Ag/AgCl

Figure 3.13 DC image of the photoanode (a) before and (b) after measuring

Figure 3.14 Time-dependent UV-vis absorbance of the photodegradation of methylene blue dye for (a) CdSe/P25 and (b) GQDs/CdSe/P25 electrodes. (c) Comparison of photocatalytic activity of two devices

List of Tables

Table 2.1 Measured sheet resistances on the FTO substrate at 750 °C

Table 2.2 BET surface area, pore volume and average pore diameter of GIO and α -Fe₂O₃/GIO

Table 3.1 EIS responses of CdSe/P25 and GQDs/CdSe/P25

Chapter 1. Introduction of Photo-electrochemical (PEC) Cell.

1.1 Hydrogen: fuel of the future

Hydrogen energy is broadly considered for the fuel of the future. According to a survey of Korea energy economics institutes, hydrogen is expected to increase sharply in 2030 as a start as show in Figure 1.1

Consequently, many efforts about the development of numerous technologies on the basis of the hydrogen applications in place of fossil have fuels due to the following reasons:

- The using of fossil fuels is in charge of climate change¹⁻⁵
- Deposits on fossil fuels are restricted
- The cost on the fossil fuels is sharply increasing;
- There is a need for a fuel made from the raw materials that are plentifully accessible
- It is necessary to be a need for a fuel that is environmentally safe

Hydrogen energy has a lot of potential applications, such as the domestic heating, powering of nonpolluting vehicles, and aircraft. Therefore, hydrogen, as an energy carrier, is expected for joining photovoltaic electricity as the source of renewable energy system.^{1,2,6} Recent effort for the development of vehicles powered by hydrogen, either directly or by hydrogen fuel cells, may possibly work for examples of how close is the hydrogen age. The diagram in Figure 1.2 shows that, while the introduction of fuel cell technology will lead to a substantial reduction in the emissions of greenhouse gases (expressed in carbon units per kilometer), the use of fuel cells powered by hydrogen obtained from solar energy will reduce the emission to nearly zero.⁵ Hydrogen is not show in environment in a vaporous form. However, it is abundantly available in water. Therefore, hydrogen must be extracted from these compounds. Thus far, hydrogen gas has been created primarily by methane gas by using vapor reorganizing.^{1,6} Nevertheless, this skill causes the production of carbon dioxide. Similarly, the hydrogen gained via water electrolysis by using electricity achieved with the burning of fossil fuels cannot be deliberated to be environmentally kindly for the identical goal. Conversely, the use of photoelectricity is reflected to be the non-toxic route for hydrogen production. Further, such hydrogen represents a storable fuel that is produced from a non-storable source of energy (photo-electricity).

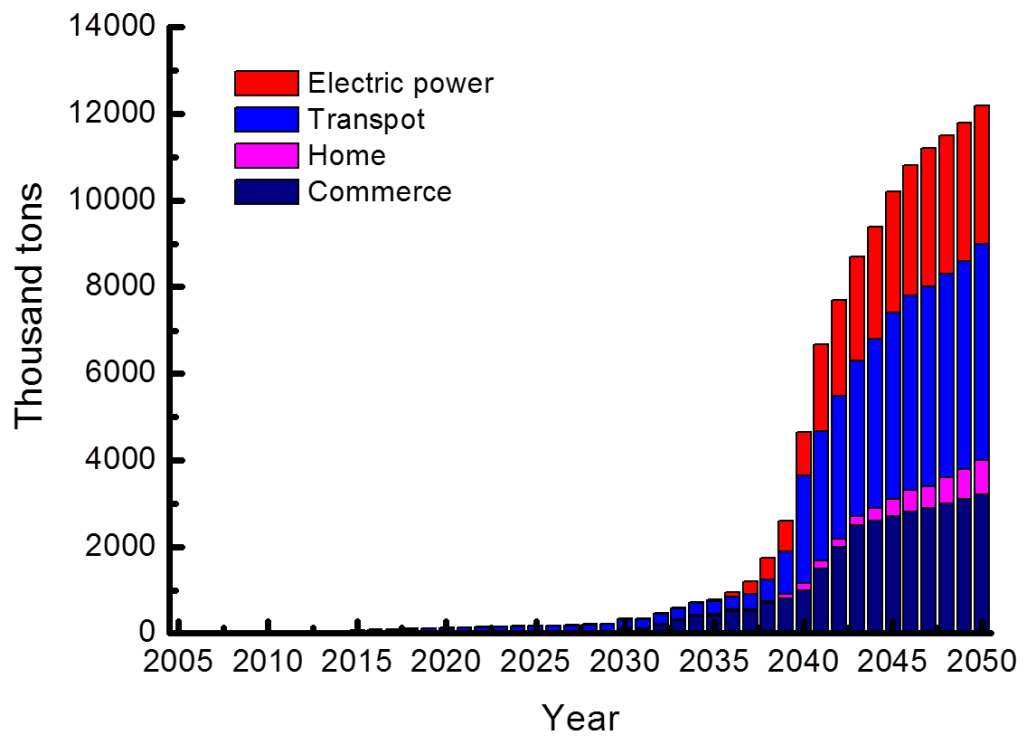


Figure 1.1 Future prospects of hydrogen energy use

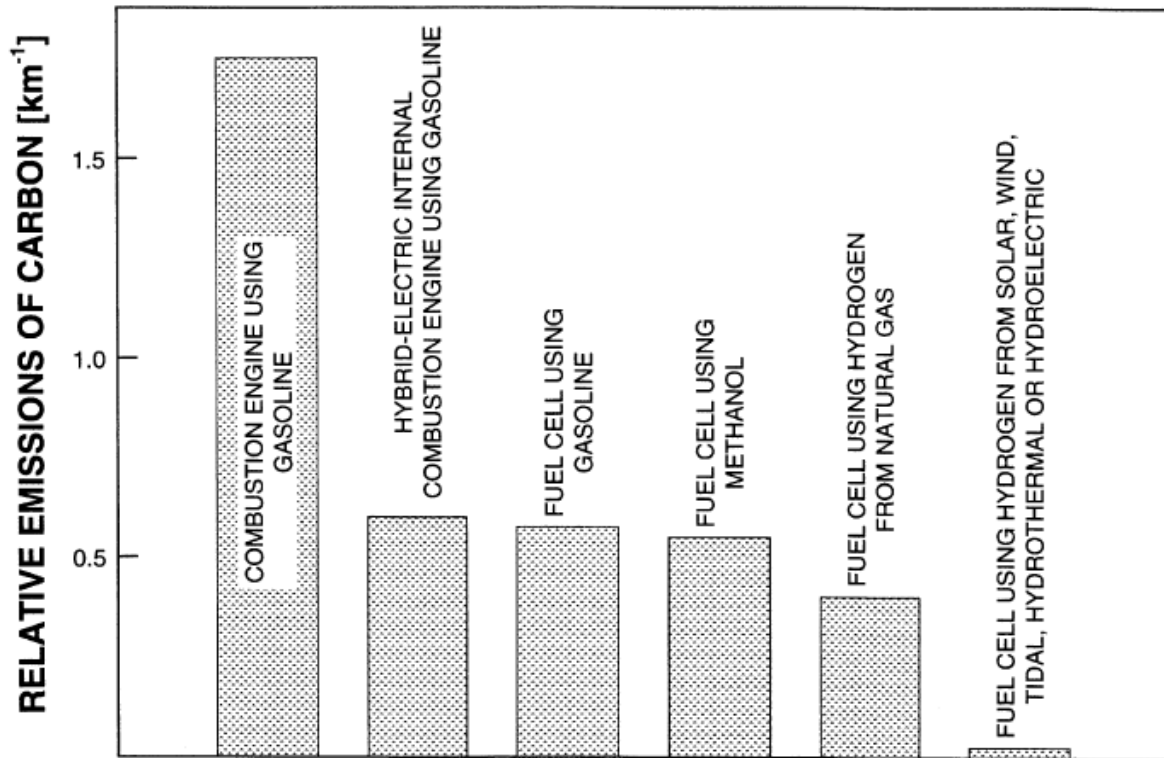


Figure 1.2 comparative emission of polluting gases (stated in carbon units per km) for vehicles motorized by today's internal combustion engine using gasoline energy compared to vehicles powered by fuel cells.

1.2 Hydrogen generation using solar energy

The general desire for the usage of hydrogen energy like as an environmentally kindly fuel has been considered by the detail that the burning of hydrogen energy causes the production of water, which neither causes air pollution nor results in the emission of polluting gases. This consideration is correct-assuming that hydrogen is generated using a source of renewable and clean energy, like as solar, wind, hydroelectric, or hydrothermal energy source. To date, the technologies for hydrogen generation using sources of renewable energy are in the incubation stage. The growing interest in hydrogen has resulted from the increasing need to develop hydrogen technologies that are based on the operation of renewable and clean energy sources. The nations having access to technologies are likely to form the OPEC of the near-future. Therefore, the development of hydrogen generation technologies based on sources of renewable energy is expected to demand substantial support from both government programs and major energy producers. There is a large body of literature that indicates that the great hopeful system of hydrogen production by using a renewable energy source is that created on photoelectrochemical water splitting by using solar source.⁷⁻¹⁵ Since first reports of this method published by Honda et al.⁷⁻¹⁰ almost 40 years ago, there have been many papers issued on the impact of diverse structures and materials for the performance of photoelectrochemical cells. The solar to hydrogen conversion effectiveness for water photo-splitting is decided primarily by the things of the materials used for photoanodes. Consequently, potential applications for hydrogen production by water and solar energy will be discovered by the progress in engineering and materials science applied to the promising candidate materials for photoelectrodes as show in Figure 1.3

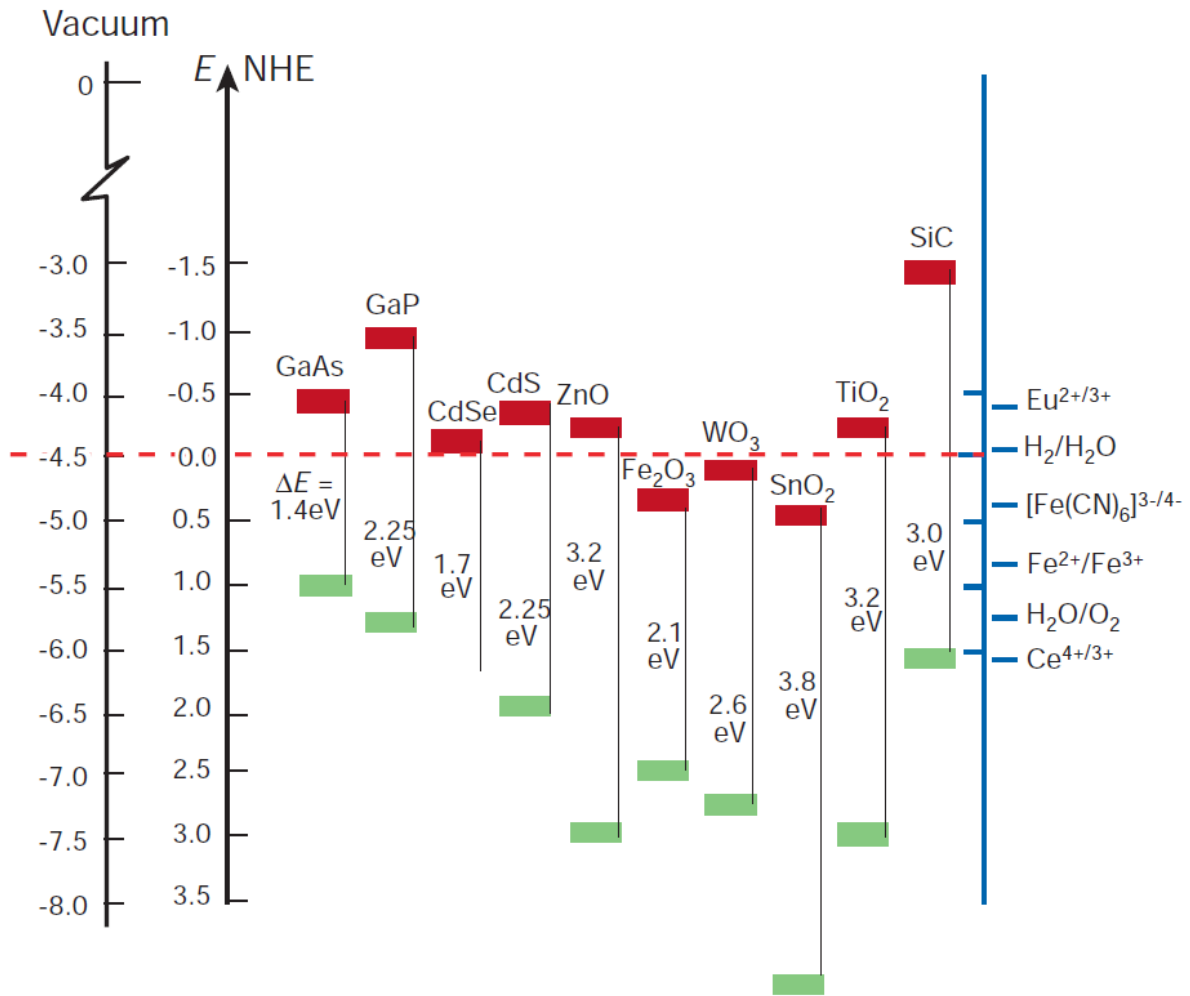


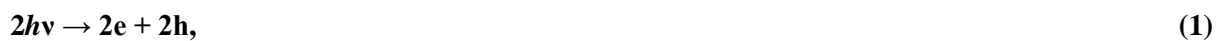
Figure 1.3 Candidate materials for photoelectrode

1.3 Reaction mechanism of photoelectrochemical cell

Photoelectrolysis of water using a photoelectrochemical cell contains several processes in photoelectrodes and at the photoelectrode/electrolyte interface, including:

- Light-brought inherent ionization in the semiconducting materials (the photo-anode), making the creation of electrical charge carriers (photoexcited electrons and holes pairs)
- Water Oxidation in the photoanode by photoexcited holes
- H⁺ ions Transport from the photo-anode to the cathode by the electron transport and electrolyte from photoanode to the cathode via the external circuit
- Hydrogen ions reduction in the cathode through electrons

Light causes inherent n-type semiconductor ionization over the band gap, resulting in the electron formation in the conduction band and holes in the valence band:



Where h is the Planck's constant, ν the frequency, e the electron, h the electron hole.

Reaction (1) can occur when the photons energy ($h\nu$) is the same to or larger than the band gap. An electric ground at the electrolyte/material surface interface is considered to avoid charge carriers recombination. This can be reached by adjustment of the potential at the electrolyte/material surface interface. The photo-excited holes result in the water splitting molecules into vaporous oxygen and hydrogen ions:



This reaction occurs between the photoanode and electrolyte interface. Oxygen gas goes forward at the photoanode and the hydrogen ions go forward to the counter electrode (cathode) over the internal route (aqueous electrolyte). At the same time, the electrons made as Reaction (1) result in the photoanode, are moved by the external route to the counter electrode, indicating the hydrogen ions reduction into vaporous hydrogen:



Therefore, the total mechanism of the photoelectrochemical cell can be stated by this form:



Reaction (4) occurs when the photon energy engaged by the photoanode are the same to or larger than E_i , the threshold power:

$$E_i = \Delta G^{\circ}_{(\text{H}_2\text{O})}/2N_A \quad (5)$$

Where $\Delta G^{\circ}_{(\text{H}_2\text{O})}$ is the free standard enthalpy per Reaction (4) mole = 237. 141 kJ/mol; N_A = Avogadro's number = $6.022 \times 10^{23} \text{ mol}^{-1}$. So, this yields:

$$E_i = h\nu = 1.23 \text{ eV} \quad (6)$$

Along with Eq. (6), the electrochemical water splitting is likely when the electromotive energy in the cell is the same to or larger than 1.23 V. The record normally considered material for the photoanode is titanium dioxide.⁷⁻¹⁰ Despite of its large band gap of 3.2 eV, it is the favored material owing to its high corrosion resistance. The maximal value obtained for the photo-voltage of a photoelectrochemical cell equipped with a photoanode of TiO_2 is $\sim 0.7\text{-}0.9 \text{ V}$.¹² Therefore, at present, the application of this material as a photoelectrode needs a bias to split water by one of the following procedures:

- Imposition of an outer bias voltage
- Imposition of an inner bias voltage by the use of various concentrations of hydrogen ions
- Imposition of an inside bias voltage by the usage of a photovoltaic part in conjunction in the photoanode (hybrid electrode)¹⁷

A photoelectrochemical cell for the photoelectrolysis of water are presented in Figure 1.4. A normal cell includes in both a photoanode (made by oxide material) and cathode (made by Pt) dipped in an aqueous salt solution (electrolyte). The procedure causes hydrogen and oxygen evolution in the photoanode and cathode, separately. The associated charge transport includes the relocation of hydrogen ions in the salt solution and the electrons transport in the outside circuit.

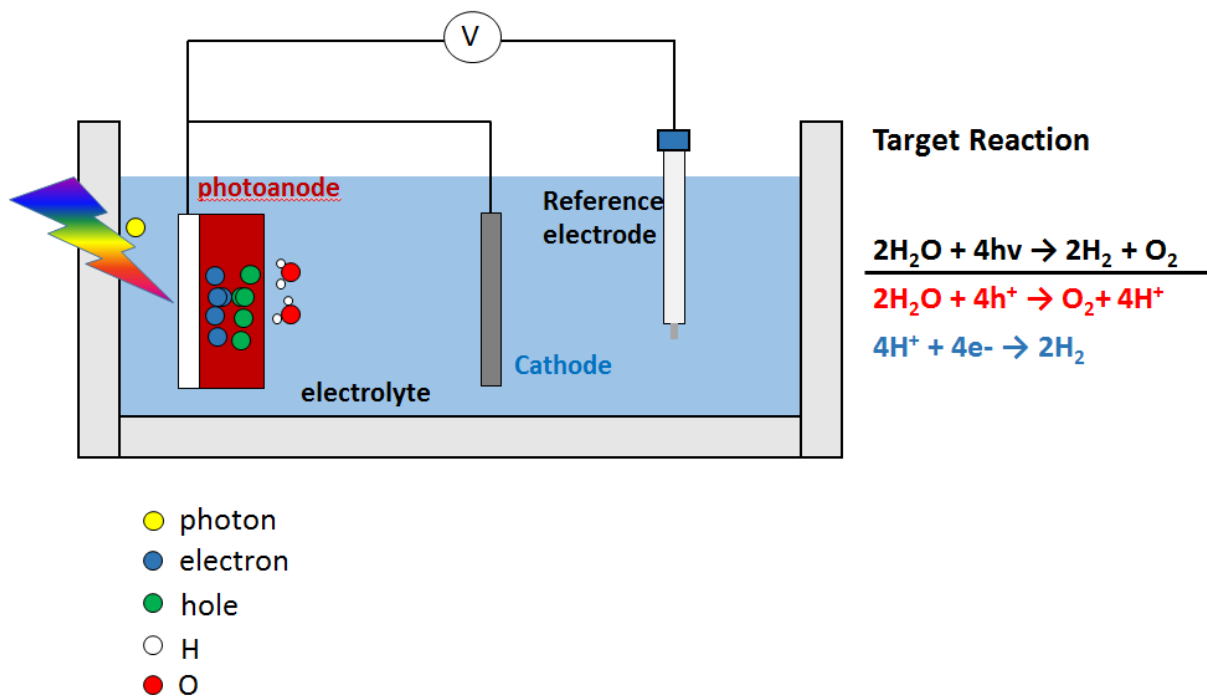


Figure 1.4 The system of photoelectrochemical cell for water photoelectrolysis.

1.4 References

1. Morgan, D.; Sissine, F., Congressional Research Service, Report for Congress, The Committee for the National Institute for the Environment, Washington, DC 20006-1401, April 28 **1995**.
2. Nejat Veziroglu, T., *Int. J. Hydrogen Energy* **1998**, 23, 1077.
3. Szyszka, A., *Int. J. Hydrogen Energy* **1998**, 23, 949.
4. Mitsugi, C.; Harumi, A.; Kenzo, F., *Int. J. Hydrogen Energy* **1998**, 23, 159.
5. The Economist Technology, Quarterly, March 25, **2001**, 29.
6. US Department of Energy, National Renewable Energy Laboratory, Hydrogen the fuel for the future, DOE/GO-1-95-099 DE95004024, March **1995**.
7. Fujishima, A.; Honda, K., *Nature* **1972**, 283, 37.
8. Watanabe, T.; Fujishima, A.; Honda, K., *Chem. Lett.* **1974**, 897.
9. Fujishima, A.; Kohayakawa, K.; Honda, K., *J. Electrochem. Soc.* **1975**, 12, 1487.
10. Honda, K.; Ohta, T., *Solar-Hydrogen Energy Systems* **1979**, 69.
11. Yoneyama, H.; Sakamoto, H.; Tamura, H., *Electrochem. Acta.* **1975**, 20, 341.
12. Ohnishi, T.; Nakato, Y.; Tsubomura, H., *Ber. Bunsenges. Phys. Chem.* **1975**, 79, 523.
13. Mavroides, J.; Tchernev, D.; Kafalas, J.; Kolesar, D., *Mater. Res. Bull.* **1975**, 10, 1023.
14. Nozik, A. *Nature* **1975**, 257, 383.
15. Hodes, G.; Cahen, D.; Manessen, J., *Nature* **1976**, 260, 312.
16. Wrighton, M.; Ellis, A.; Wolczanski, P.; Morse, D.; Abrahamson, H.; Ginley, D., *J. Am. Chem. Soc.* **1976**, 98, 2774.
17. Morisaki, H.; Watanabe, T.; Iwase, M.; Yazawa, K., *Appl. Phys. Lett.* **1976**, 29, 338.

Chapter 2. Hematite-Based Photo-electrochemical cell Supported by Graphene Inverse Opal Structures

2.1. Introduction

Water splitting of photo-electrochemical (PEC) cell using semiconductor for solar energy to hydrogen production has obtained intensive focus in the decades.¹ Of many semiconducting materials, α -Fe₂O₃ is a stable, promising n-type and earth-abundant material for PEC cell because of a suitable band gap 2.1~2.2 eV in the visible range.²⁻⁴ Some critical problems stay to be treated for efficient α -Fe₂O₃ to be widely used for a photo-electrode in photo-electrochemical device: its short hole diffusion length (2-4 nm), indicating that causes a high recombination; low absorption by indirect band gap near the band edge, and bulk/surface faults⁵ which result in the low hole mobility and high over-potential. Many research such as nano-structuring,⁶⁻⁷ impurity doping,⁴ making surface treatment with IrO₂ and Co-Pi⁹⁻¹⁰ and a heterojunction⁸ have been strived hard to resolve these problems in α -Fe₂O₃ based photo-electrochemical cells. New promising method to resolve problems would be to quickly and directly transfer photo-excited electrons made in photo-electrodes to a three-dimensional (3D) electrode with light scattering effects.

A three-dimensional nano-network structure has received substantial attention as a conducting electrode for energy related fields because of large surface area allowing sites of reachable vigorous areas, bicontinuity and short distance contact improving the transport of charge carriers.¹¹⁻¹⁴ Graphene for a conductive electrode has excellent prospective because of its fast electron conductivity, flexible and transparent properties.¹⁵⁻¹⁶ Former efforts have been suggested to increase photo-catalytic action with the graphene incorporation with good catalytic properties as well as excellent conductivity. Nevertheless, many methods presented relatively minor improve in photo-catalytic action using chemically made graphene sheet. Of many available techniques to make the graphene preparation, chemical vapor deposition (CVD) development of graphene with a silica or metal coated a silicon substrate is currently an excellent method to make large area and high quality for graphene.¹⁷⁻¹⁸ Nonetheless, limitation made by the CVD growing condition of high temperature, about 1,000 °C, affects the select of substrate, indicating might importantly decide the device performance. For instance, FTO glass, used for a conductive substrate, has been asked as a substrate growing graphene, because FTO is unsteady at high temperature because FTO glass has the low melting temperature. Thus, developing a method to create graphene directly on the FTO substrate, that removes the transfer process, would carry powerful advantage with the practical and broad use of graphene. Herein, we story a 3D nano-network graphene of new type for conductive electrode that is grown on FTO glss at low temperature of 500 °C by cabon source on a 3D-Nickel inverse opal (NIO) surface. α -Fe₂O₃

nanoparticles (NPs) were attached on 3D nano-network graphene inverse opal (GIO) by hydrothermal method for efficient hydrogen production. a 3D nano-network α -Fe₂O₃/GIO showed 1.4 times increased performance relative to α -Fe₂O₃ at 1.5 V bias, that can be featured to the straight transfer of photogenerated electrons in α -Fe₂O₃ to 3D nano-network structure graphene conductive electrodes by direct and short interaction.

2.2 Experimental and characterization

2.2.1 Preparation of Graphene Inverse Opal (GIO)

350 nm polystyrene (PS) beads were synthesized by emulsion polymerization: 0.96 M of a styrene (Aldrich) as monomer, 19 mM of an azobisisobutyronitrile (Aldrich) as initiator and 300 μ M of PVP 40 K (Aldrich) as stabilizer in deionized (DI) water were used without any purification for a 24 hrs reaction time. A fluorine-doped tin oxide (FTO) substrate was applied to make a square by scotch tape with an area of 5 mm X 5 mm. The synthesized PS beads were dispersed in ethanol (5 wt%) and then PS beads was assembled by spin-coating the dispersed solution onto the FTO substrate at 1,000 rpm for 60 sec. the height of the PS beads coated in this experiment was about 5 μ m. Then electrodeposited into PS opal structure in a solution of NiSO₄·6H₂O (Aldrich), NiCl₂·6H₂O (Aldrich) and H₃BO₃ and 100 g DI water and diluted four times. The conditions of electrodeposition were 5 mA for 2 min. The PS opal structures were dissolved in toluene for 6 hrs. For the growth of graphene, Nickel oxide on FTO was carburized in triethylene glycol (Aldrich) at 250 °C 12 hrs. The prepared samples were annealed in a furnace at 500 °C for 1 hr with an argon atmosphere, resulting in graphene/NiO. GIO was obtained by etching the nickel in ammonium persulfate solution for 12 hrs.

2.2.2 Preparation of pristine to α -Fe₂O₃ and to α -Fe₂O₃/GIO

For the synthesis of β -FeOOH NPs on GIO, the GIO on FTO was immersed in 10 ml of FeCl₃·6H₂O (25 mM) aqueous solution and kept in a convection oven with ramp rate of 1 °C/min for 4 hrs at 75 °C. The samples were washed with DI water and EtOH. Finally, β -FeOOH/GIO was heated by a two-step annealing process at 350 °C for 4 hrs on a hot plate under an air condition and at 750 °C for 1 hr in furnace under Ar atmosphere with a ramp rate of 10 °C/min, and was naturally cooled down to room temperature while maintaining and Ar atmosphere. The pristine α -Fe₂O₃ was prepared from β -FeOOH NPs by following recently published paper.

2.2.3 Photo-electrochemical measurement

The PEC action in the α -Fe₂O₃/GIO electrodes was played in a three-electrode system under front side illumination of AM 1.5 G. An Ag/AgCl electrode and a Pt mesh were used as reference and counter electrodes, respectively. 1 M NaOH was used as an electrolyte. The exposed area of the working electrode was fabricated to have an exact value of 0.25 cm² by scotch tape. Photocurrent stability tests were carried out by measuring the photocurrent produced under chopped light irradiation (light/dark cycles of 10 sec) at a bias 1.5 V versus RHE. Electrochemical impedance spectroscopy (EIS) was carried out at a frequency range from 100 kHz to 0.1 Hz using a potentiostat at a bias 0.5 V versus open circuit potential under illumination. The incident photon-to-electron conversion efficiency was measured at a bias of 0.5 V versus open circuit potential.

2.3 Results and Discussion

α -Fe₂O₃/GIO was organized via the subsequent four steps, such as illustration in Figure 2.1. Firstly, 350nm PS beads made by emulsion polymerization were made into structures of 3D opal on FTO substrate, next, by electro-deposition method of nickel on the opal structures of polystyrene (Figure 2.2). The PS dimension was decided to powerfully light scattering for well-organized light trapping as reported at our former reports. Secondly, the opal structure of polystyrene was removed in toluene, saving inverse opal structures of the nickel. Third, the as-prepared nickel IO was carburized using triethylene glycol solution with the assistance of catalytic Nickel at 250 °C for 12 hrs. Through the following CVD method at 550 °C under Ar condition for 1 hr, dissociated carbon percolated down through the nickel IO structure. The carbon source segregated from the carbon-dissolved NIO structure throughout the cooling procedure, making a 3D nano-network graphene structure on 3D-nickel IO surface. By removing nickel IO structures, a 3D nano-network graphene structures having a 350 nm diameter was made. Finally, α -Fe₂O₃/GIO of High crystalline was gained by annealing the β -FeOOH NPs/GIO via two steps (350 °C under air and then 750 °C under Ar). The conductivity of FTO glass handled under this experiment is shown in Table 2.1. The heat-treated temperature of 750 °C was adjusted for the photo-anode to get the best crystallinity as shown in Figure 2.3. Figure 2.4a shows a scanning electron microscope (SEM) image of GIO. Due to the highly soluble carbon source of Ni, multi-dimensional graphene was made, that approves with results of supplementary related research. It should be renowned that the 3D nano-network graphene were not substantially collapsed and physicochemical things of low temperature-growing our 3D nano-network graphene, such as transparency (59% at 550 nm), and conductivity (1.4 k Ω / \square), were not significantly poorer to other thing of growing graphene at 1,000 °C. A SEM image of α -Fe₂O₃ attached on 3D nano-network graphene surface is presented in Figure 2.4b. The element mapping data are presented in Figure 2.5. Importantly, we targeted α -Fe₂O₃ NPs with less than 10 nm diameter, which confirm a short hole diffuse length to the apparent of hematite, as well as enlarged surface part to reward the relatively low energetic area on the larger 3D dimension nano-network graphene surface. The surface active sites was carried out via nitrogen adsorption-desorption isotherms using 0.2 g and 0.5 g of graphene and α -Fe₂O₃/GIO respectively. A plot of relative pressure vs. volume absorbed was gained by calculating the amount of N₂ gas that attach on the area of the subsequent and interest amount that detach at a 70 K constant temperature. The surface active sites of α -Fe₂O₃/GIO was increased up to 63 m²/g after α -Fe₂O₃ attachment, that is four times than 15 m²/g of 3D nano-network graphene surface in shown Figure 2.6 and Table 2.2. The details on adjusting the dimension of β -FeOOH NPs can be establish in Figure 2.7. The well-arranged pores in Figure 2.4b identify α -Fe₂O₃/GIO keeps the unique IO structures without excessive bend. In Figure 2.4c and 2.4d, the transmission electron microscopy

(TEM) images reveal high density α -Fe₂O₃ NPs using lengths of around 10 nm on the ~10 layers graphene surface with α -Fe₂O₃/GIO. The certain sites electron diffraction (SAED) patterns of α -Fe₂O₃ NPs in the supplement of Figure 2.4c are shown with the graphene pattern, indicating the attachment of α -Fe₂O₃ NPs on 3D nano-network graphene surface was occurred. The supplement in Figure 2.4d presents the high crystalline α -Fe₂O₃ zoomed-up image with 0.25 nm spacing of lattice, matching to the (110) plane. The formation of GIO and α -Fe₂O₃ NPs onto the sites of 3D nano-network was identified via Raman analysis and XRD data. The many peaks of α -Fe₂O₃ at 33.5°, 35.92° and 64.3°, matching to the (104), (110) and (300) planes (JCPDS 99-000-1511) performed in the XRD of α -Fe₂O₃/GIO. α -Fe₂O₃ gained by using a single step annealing condition at 750 °C under an Ar atmosphere caused in the a mixture creation of Fe₂O₃ and Fe₃O₄ as shown in Figure 2.8. The normal graphene position at 26° matching to the (002) plane, that was created onto the surface of nickel IO via CVD at 500 °C, was not identified in the XRD data because of the overlay with the tough peak of FTO glass at 27°. As an alternative, the graphene creation was presented via Raman data. Raman data of 3D nano-network graphene in Figure 2.9 exposed the D and G bands at about 1,350 cm⁻¹, 1,580 cm⁻¹ and the 2D band at 2,700 cm⁻¹ of graphene. The clear curve of three main peaks, 0.615 ID/IG ratios and of 0.880 I2D/IG ratios show the creation of a multi-layer graphene creation, gained at the graphene growth condition of low temperature (500 °C). The Raman spectrum with α -Fe₂O₃/GIO is shown in Figure 2.10

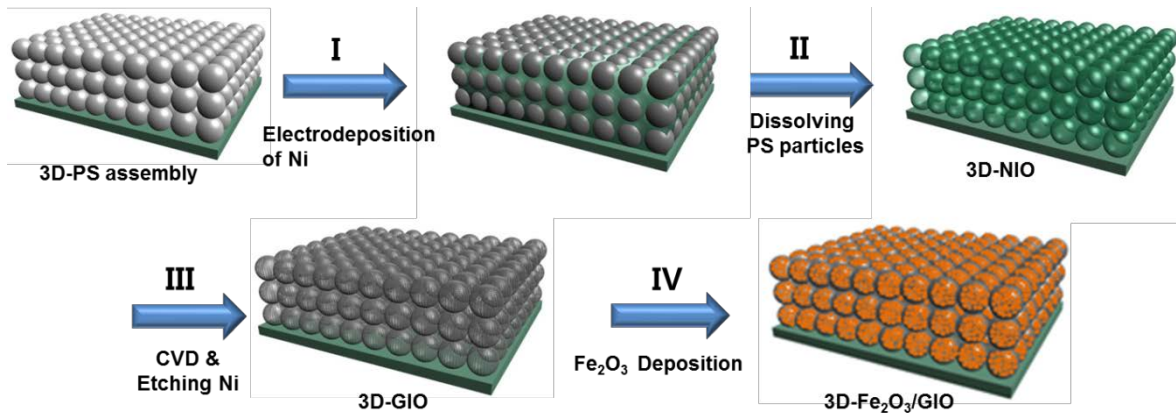


Figure 2.1 Illustration for the fabrication of $\alpha\text{-Fe}_2\text{O}_3/\text{GIO}$

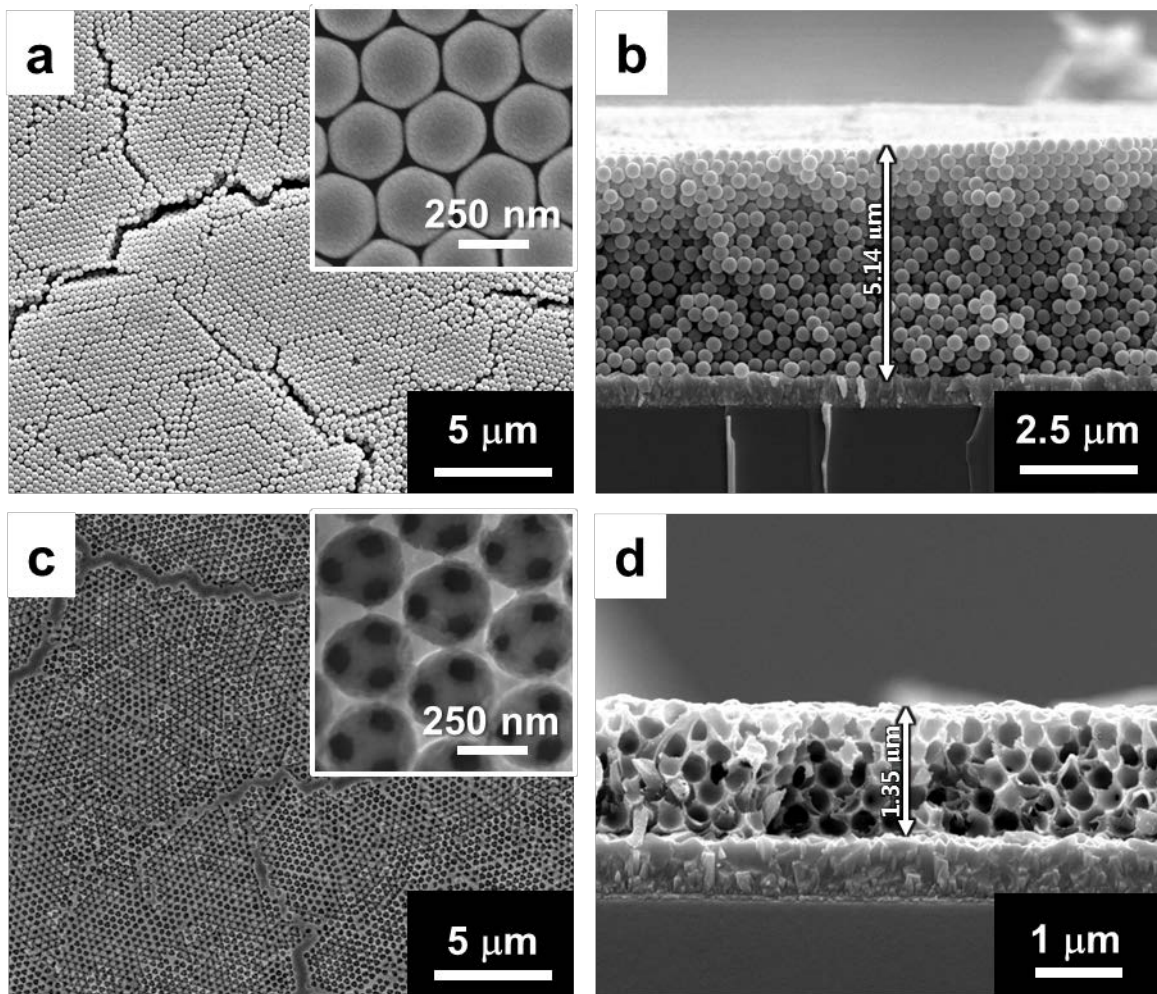


Figure 2.2 SEM images of assembled PS opal (a,b) and NIO structure (c,d).

750 °C (Ω/\square)	FTO (Ω/\square)
6.46	6.1
6.282	6.2
6.657	6.206
6.537	6.083
6.425	6.407
6.442	6.207
6.469	6.189
6.1	6.098
6.335	6.224

750 °C	N total	Mean	Standard Deviation	Sum	Minimum	Median	Maximum
A	9	6.41189	0.15908	57.707	6.1	6.442	6.657

FTO	N total	Mean	Standard Deviation	Sum	Minimum	Median	Maximum
B	9	6.19044	0.09804	55.714	6.083	6.2	6.407

Table 2.1 Measured sheet resistances on the FTO substrate at 750 °C.

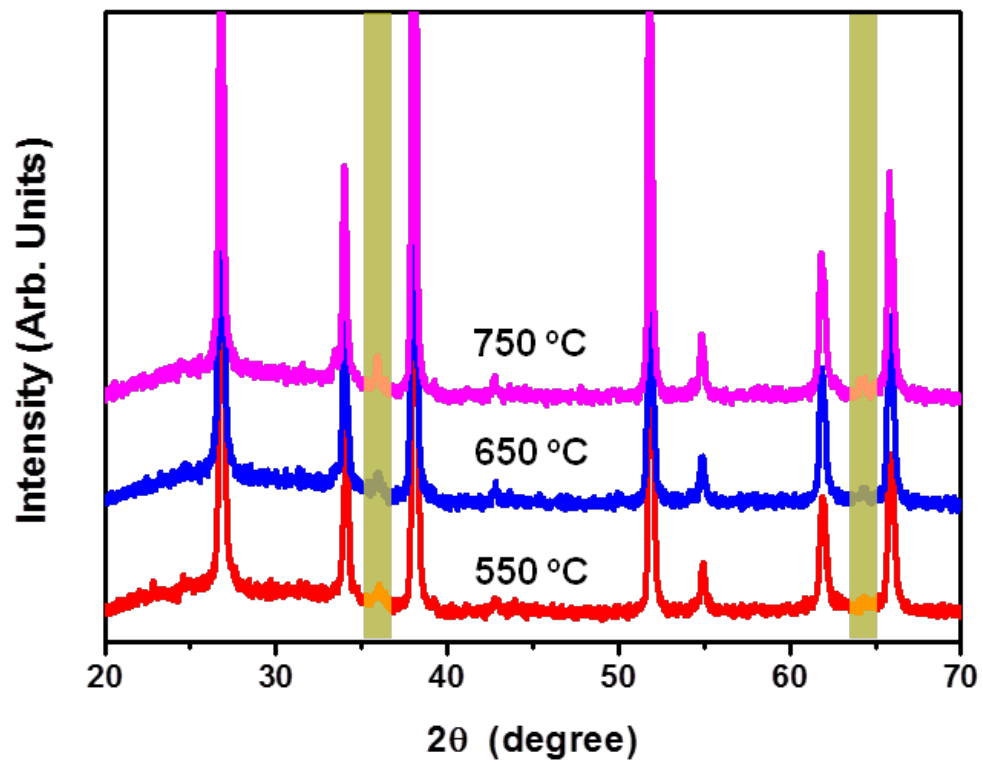


Figure 2.3 XRD analysis of $\alpha\text{-Fe}_2\text{O}_3/\text{GIO}$ with various annealing temperatures

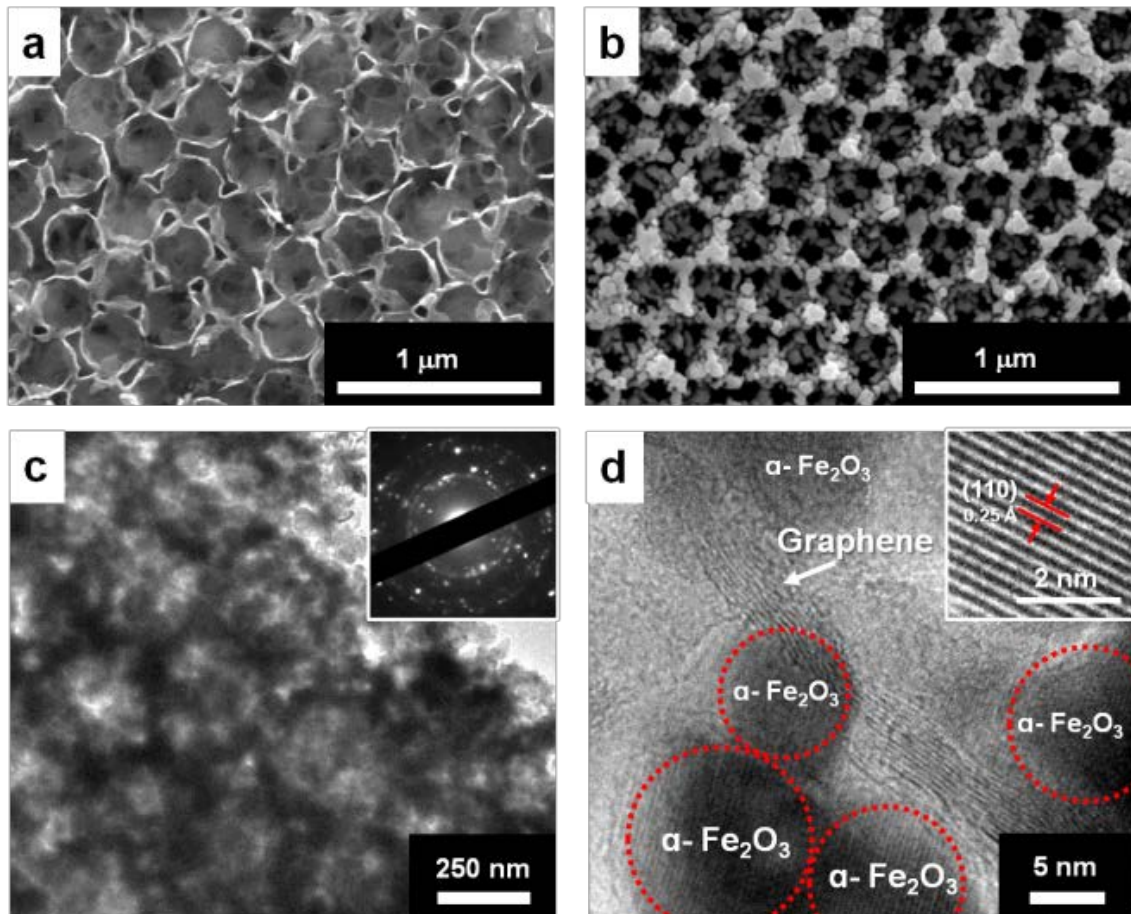


Figure 2.4 SEM images of (a) GIO after etching nickel and (b) α - Fe_2O_3 /GIO. (c-d) TEM images of α - Fe_2O_3 /GIO. The inset images in (c) and (d) are SAED pattern and (110) lattice plane of α - Fe_2O_3 , respectively.

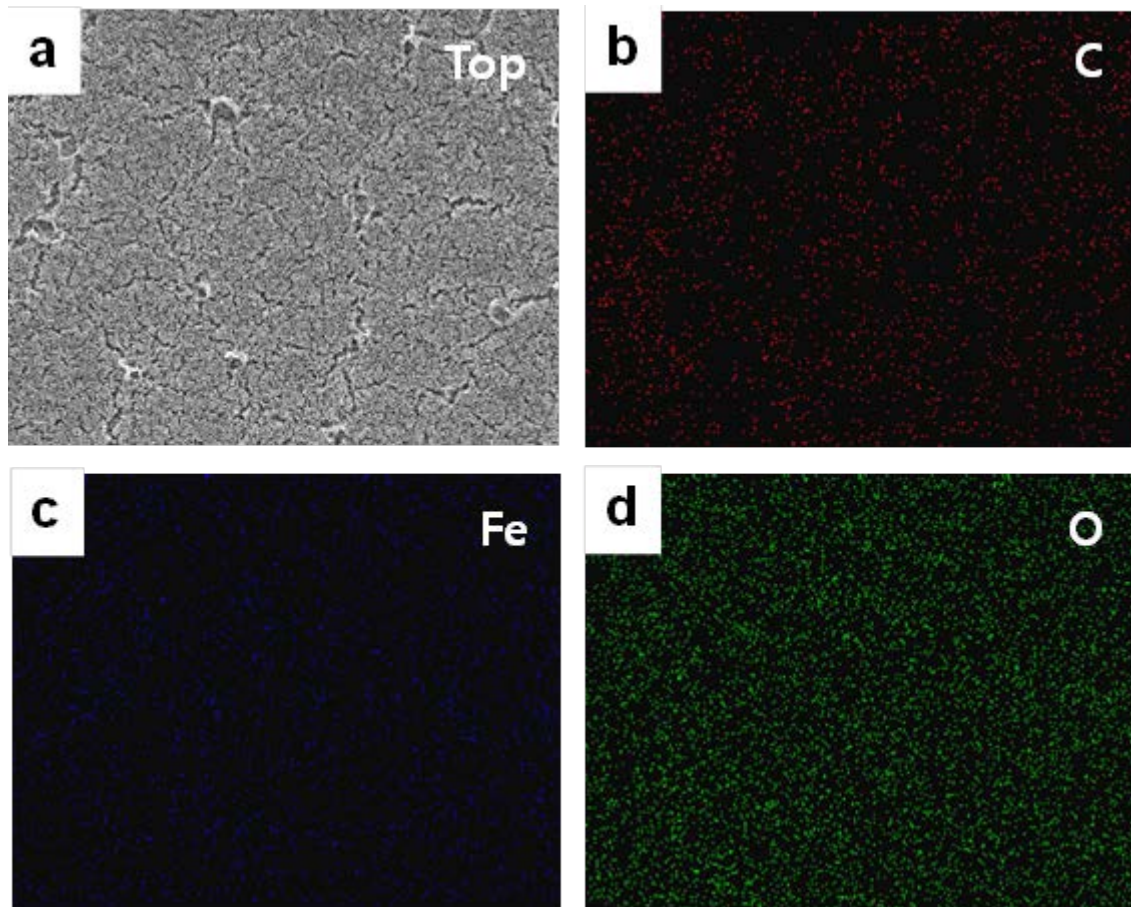


Figure 2.5 (a) Top view of SEM image and elemental mapping (b-d) for α -Fe₂O₃/GIO by SEM-EDX.

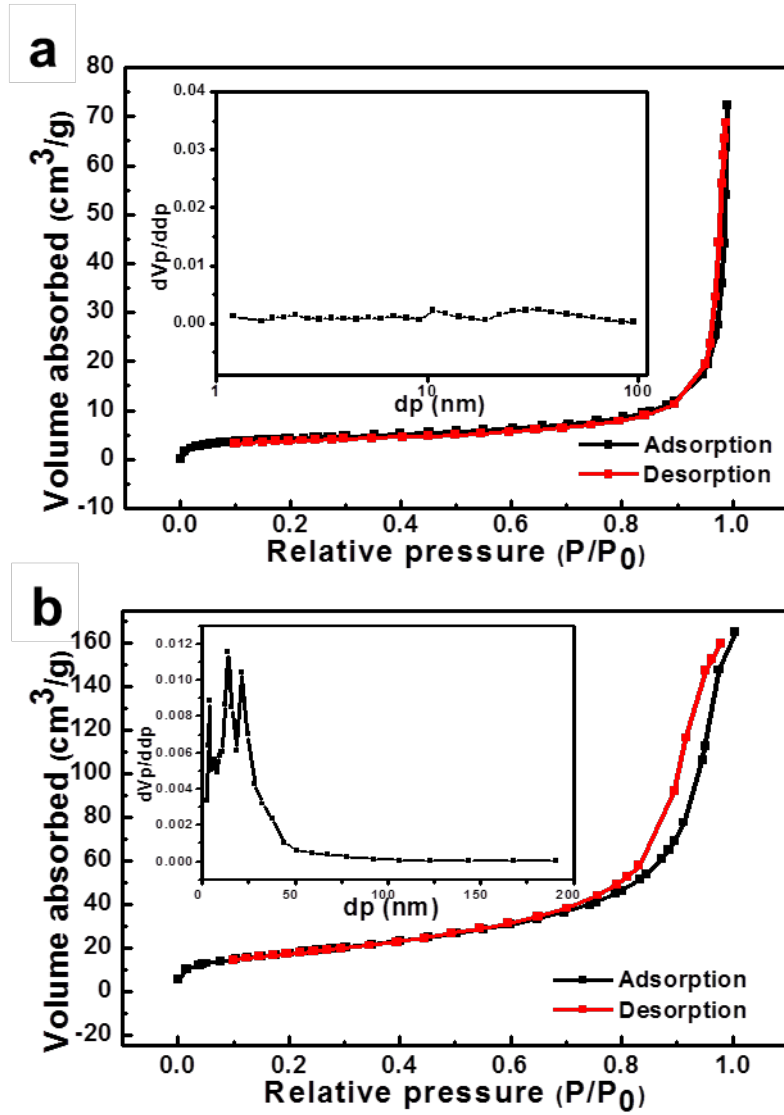


Figure 2.6 BET analysis of (a) GIO and (b) α-Fe₂O₃/GIO

	Surface area (m ² g ⁻¹)	Pore volume (cm ³ g ⁻¹)	d _{p,peak} (nm)
GIO	15.15	0.1063	33.81
Fe ₂ O ₃ /GIO	62.97	0.2416	15.346

Table 2.2 BET surface area, pore volume and average pore diameter of GIO and α -Fe₂O₃/GIO.

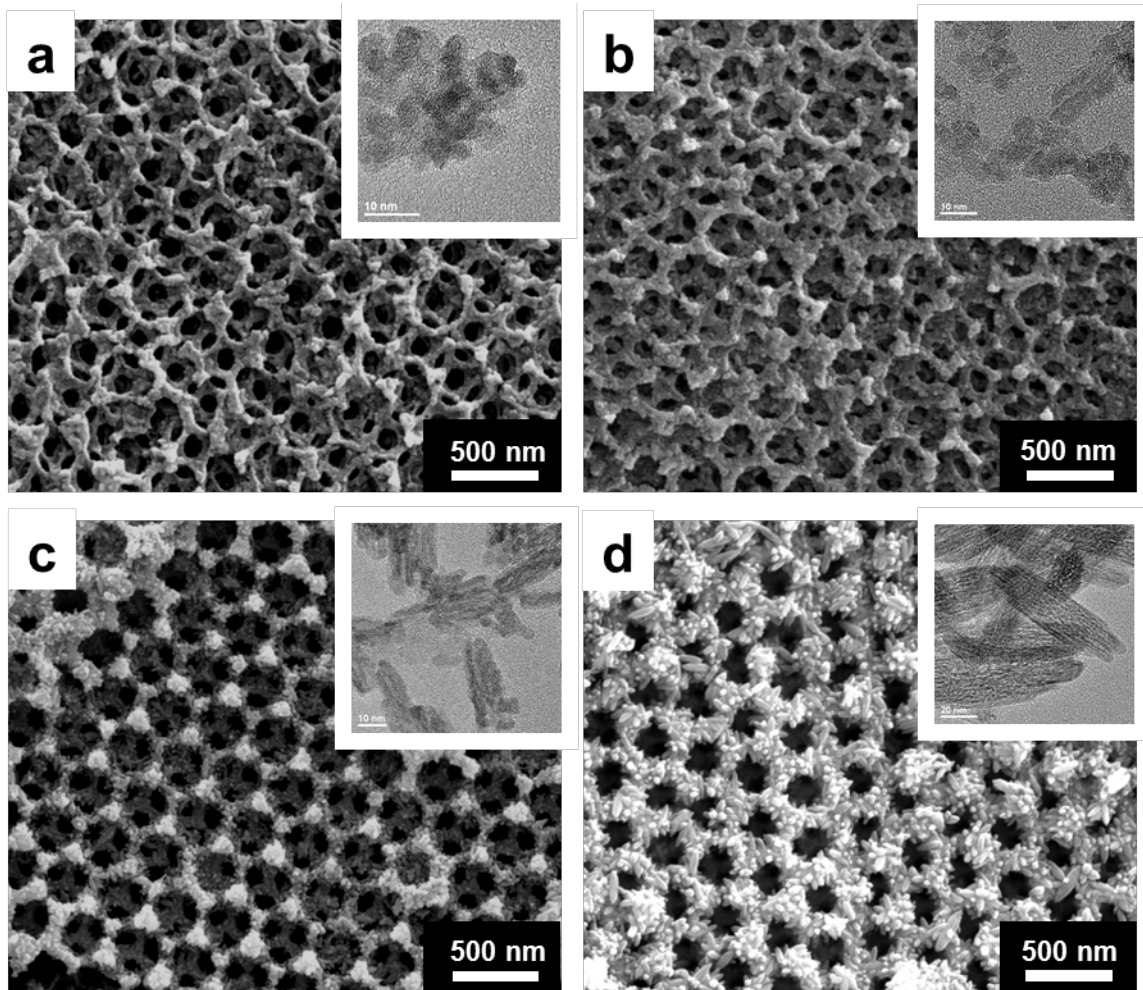


Figure 2.7 SEM images of β -FeOOH/GIO which show the variations in the size of NPs at various concentrations of $\text{FeCl}_3 \cdot 6\text{H}_2\text{O}$ solution. (a) 5mM, (b) 10mM, (c) 25mM and (d) 50 mM. The insets are the corresponding TEM images.

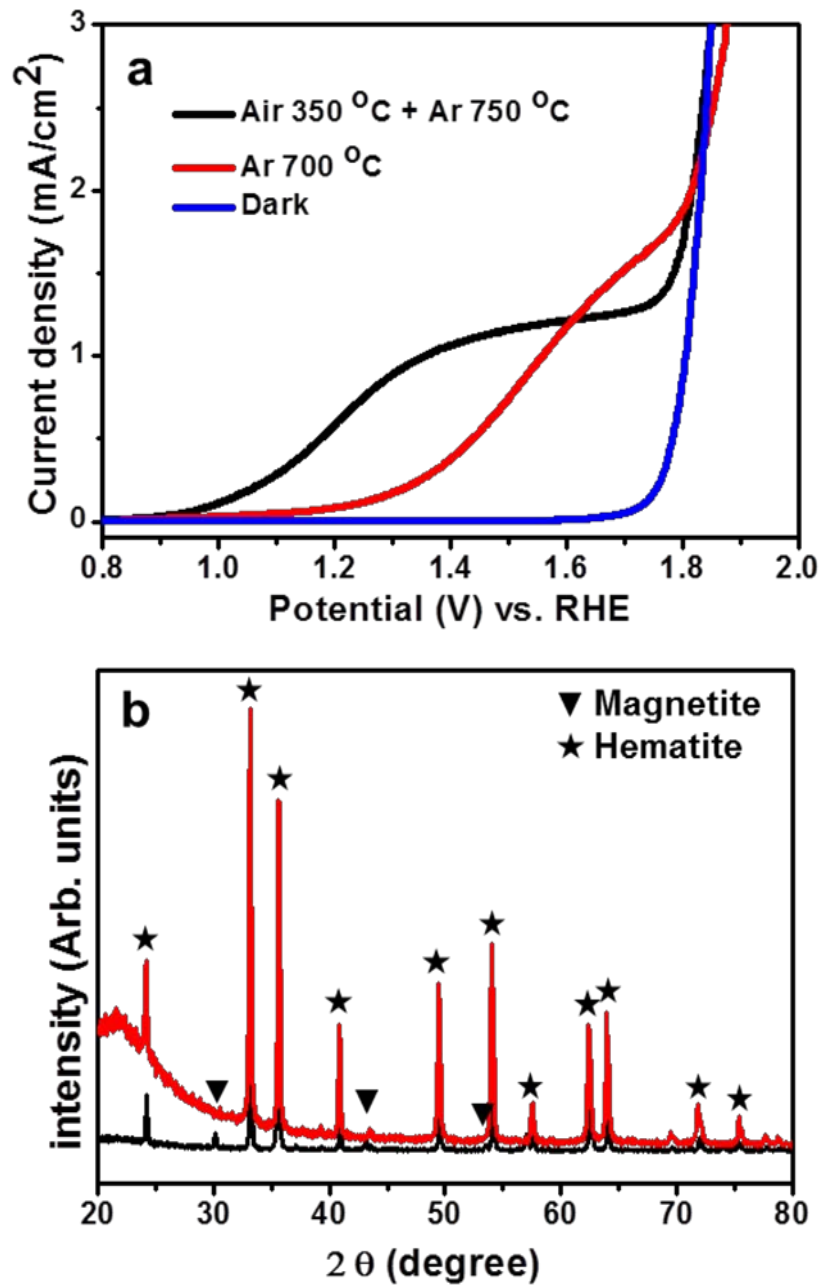


Figure 2.8 (a) photocurrent behavior and (b) XRD analysis of the samples prepared by single step annealing at 750 °C (black line) and by two-step annealing at 350 °C for 4 hrs and 750 °C for 1hr (red line).

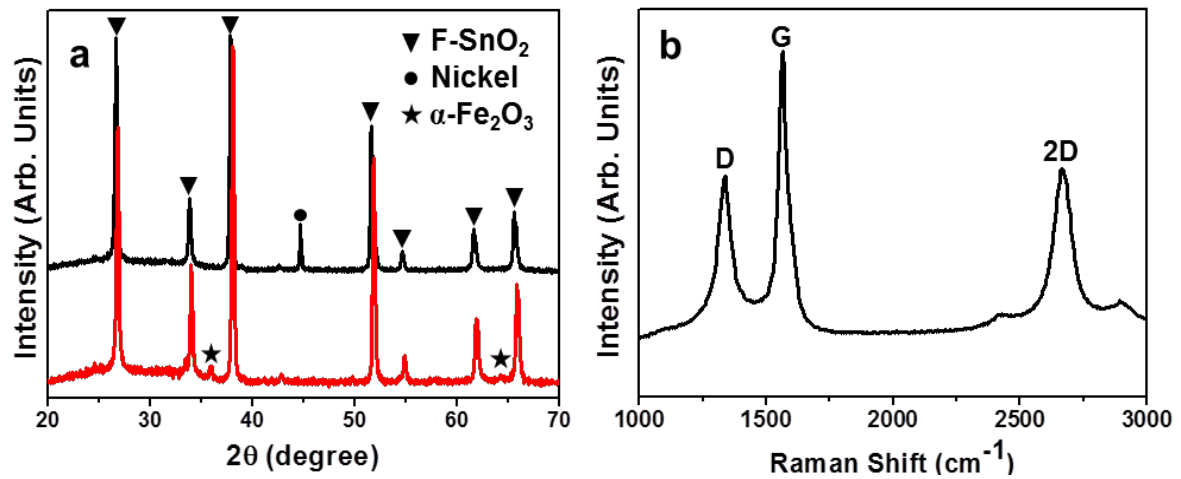


Figure 2.9 (a) XRD analysis of NIO (black line) and α -Fe₂O₃/GIO (red line) on FTO substrate. (b) Raman spectrum of GIO.

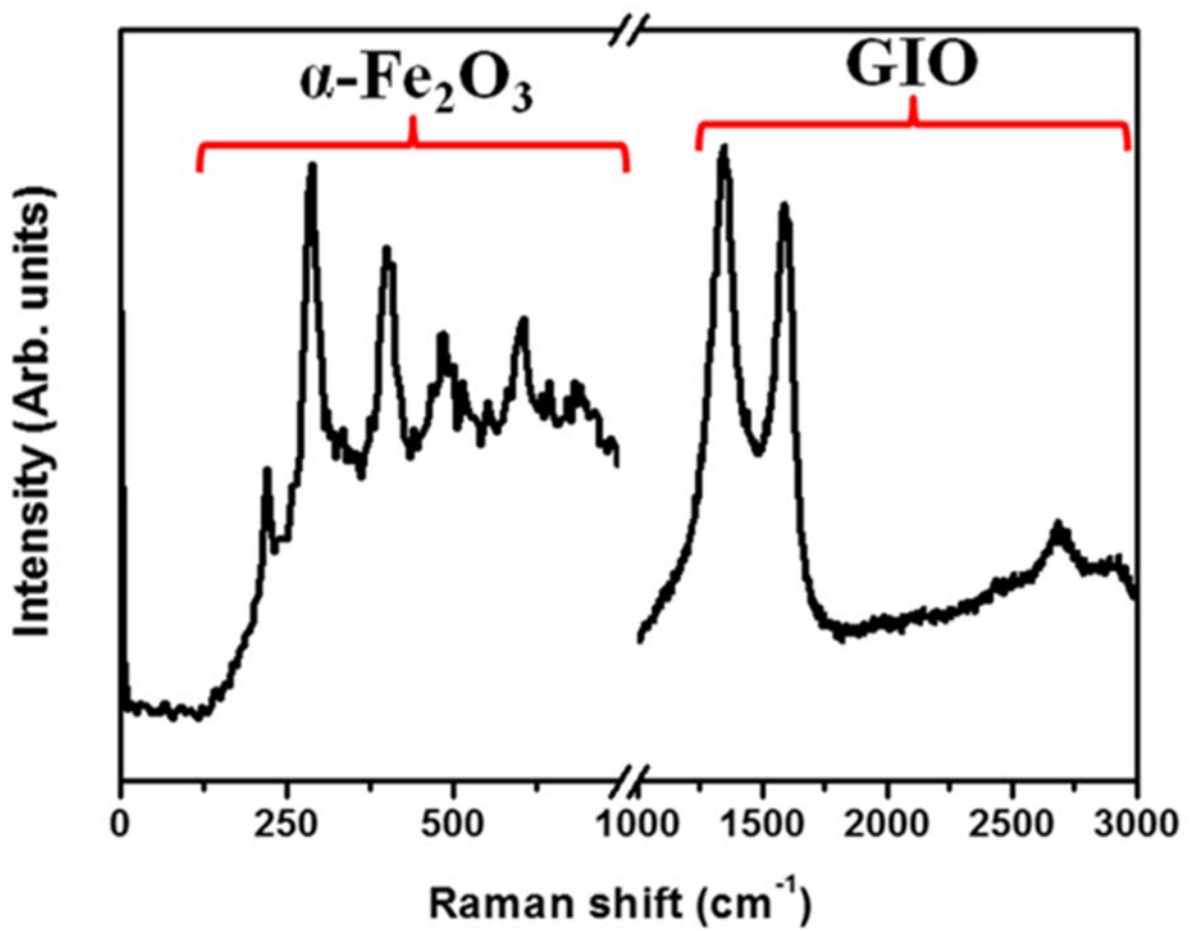


Figure 2.10 Raman analysis of $\alpha\text{-Fe}_2\text{O}_3/\text{GIO}$

We theorized that the 3D nano-network graphene efficiently offer a light collecting mechanism that theoretically improves the photo-conversion efficiency of low absorption $\alpha\text{-Fe}_2\text{O}_3$ where $\alpha\text{-Fe}_2\text{O}_3$ is poor, in the red spectral area, as stated by other inverse opal-focused researches. To study the concentration of trapped light under irradiation of light, the diffusion reflectance data of $\alpha\text{-Fe}_2\text{O}_3$ and $\alpha\text{-Fe}_2\text{O}_3/\text{GIO}$ were carried out, as shown in Figure 2.11a. Here, $\alpha\text{-Fe}_2\text{O}_3$ is a nano-sized sample with a 150 nm thickness collected of NPs made via the same technique such as the $\alpha\text{-Fe}_2\text{O}_3$ deposited on the 3D nano-network graphene surface. Compared to $\alpha\text{-Fe}_2\text{O}_3$, the $\alpha\text{-Fe}_2\text{O}_3/\text{GIO}$ shown considerably higher diffusion reflection spectrum in the 550-800 nm visible range, which the light of photo-anode absorbed was proficiently trapped in the nano-structure owing to the 3D nano-network graphene structure in the nm scale of few hundred, proving longer passages of light. The result of presenting photon scattering 3D nano-network graphene in the hematite was obviously detected by associating the Ultra violet extinction spectra of the $\alpha\text{-Fe}_2\text{O}_3/\text{GIO}$ compared with two types of samples without the photon scattering effects, that were because of the small sites of the pores (the pristine of $\alpha\text{-Fe}_2\text{O}_3$ and nano-foam graphene having pores of ~ 40 nm) as presented in Figure 2.11b. Associated to the classic absorption spectra of the $\alpha\text{-Fe}_2\text{O}_3$ and absorption spectra of the 150 nm thick nano-foam graphene that presents similar absorption values in the total spectral region, the $\alpha\text{-Fe}_2\text{O}_3/\text{GIO}$ displayed a significantly improved distinctive absorption spectrum in 450-650 nm the long wavelength section. It suggests that low absorption of $\alpha\text{-Fe}_2\text{O}_3$ NPs was the efficiently overwhelmed by $\alpha\text{-Fe}_2\text{O}_3/\text{GIO}$, that can be qualified to 3D nano-network graphene surface with the photon scattering effect. (the Tauc plot shows $\alpha\text{-Fe}_2\text{O}_3$ and $\alpha\text{-Fe}_2\text{O}_3/\text{GIO}$ a band gap in Figure 2.12). The photo-current densities of $\alpha\text{-Fe}_2\text{O}_3/\text{GIO}$ were carried out at a potential variety from 0.6 to 2.0 V under AM 1.5 G replicated light illumination, as displayed in Figure 2.13a. Compared to pristine of $\alpha\text{-Fe}_2\text{O}_3$, the photo-current density of $\alpha\text{-Fe}_2\text{O}_3/\text{GIO}$ showed excellent improvement. The pristine of $\alpha\text{-Fe}_2\text{O}_3$ showed a photo-current density of 1.17 mA/cm^2 at a 1.5 V bias vs RHE, indicating comparable to the testified values of pristine of $\alpha\text{-Fe}_2\text{O}_3$ in other readings. The maximum photo-current density of $\alpha\text{-Fe}_2\text{O}_3/\text{GIO}$ got 1.62 mA/cm^2 at 1.5 V bias vs RHE, indicating 1.4 times higher than photo-current density of pristine of $\alpha\text{-Fe}_2\text{O}_3$. This improvement can be ascribed to the direct attachment of $\alpha\text{-Fe}_2\text{O}_3$ NPs onto 3D nano-network graphene surface that enables fast electron transfer over the bicontinuous nano-networks in $\alpha\text{-Fe}_2\text{O}_3/\text{GIO}$. J-T curvature of $\alpha\text{-Fe}_2\text{O}_3/\text{GIO}$ was gained via sliced illumination of AM 1.5 G at a 10 s interval of on/off for UV-visible light at 1.5 V bias (Figure 2.13b). The quick happening and decline in the photo-current density during the on/off illumination arrangement suggests the fast transfer of photo-created electrons from $\alpha\text{-Fe}_2\text{O}_3$ to 3D nano-network graphene. To discover the $\alpha\text{-Fe}_2\text{O}_3$ electrical behavior and $\alpha\text{-Fe}_2\text{O}_3/\text{GIO}$, EIS experiment were performed at a frequency range from 100 kHz to 0.1 Hz in 1 M NaOH electrolyte and at open circuit voltage condition (Figure 2.13c). The onset point for the real axis (R_s) at the high-frequency region presents

the contact resistance and the inherent resistance of the conducting material with FTO glass. The the semicircle diameter (R_{ct}) at the middle frequency area delivers the interfacial charge transfer resistance. $\alpha\text{-Fe}_2\text{O}_3/\text{GIO}$ has a lower 36Ω R_s value than R_s value of pristine of $\alpha\text{-Fe}_2\text{O}_3$, 109Ω , that the $\alpha\text{-Fe}_2\text{O}_3/\text{GIO}$ photo-anode has lower contact resistance and better inherent conductivity than the pristine of $\alpha\text{-Fe}_2\text{O}_3$ photo-anode. This suggests a great benefit of the short-distance contact and direct of $\alpha\text{-Fe}_2\text{O}_3$ with a 3D nano-network graphene current collector. The enhancement can also be ascribed to our direct growing technique of 3D nano-network graphene on FTO glass. At the middle frequency range, the semicircle diameter of $\alpha\text{-Fe}_2\text{O}_3/\text{GIO}$ is much smaller than semicircle of $\alpha\text{-Fe}_2\text{O}_3$, indicating that $\alpha\text{-Fe}_2\text{O}_3/\text{GIO}$ offers paths for more operative charge transfer between electrodes and electrolytes and thus more reduced recombination (Figure 2.14). In Figure 2.13d, the incident photon-to-electron conversion efficiency (IPCE) of $\alpha\text{-Fe}_2\text{O}_3/\text{GIO}$ shows a maximum rate of 42 % at 320 nm with an stretched photo-response area up to 600 nm and is total much higher than IPCE value of a normal $\alpha\text{-Fe}_2\text{O}_3$ photo-anode, that more light energies have been transformed to photo-currents in $\alpha\text{-Fe}_2\text{O}_3/\text{GIO}$.

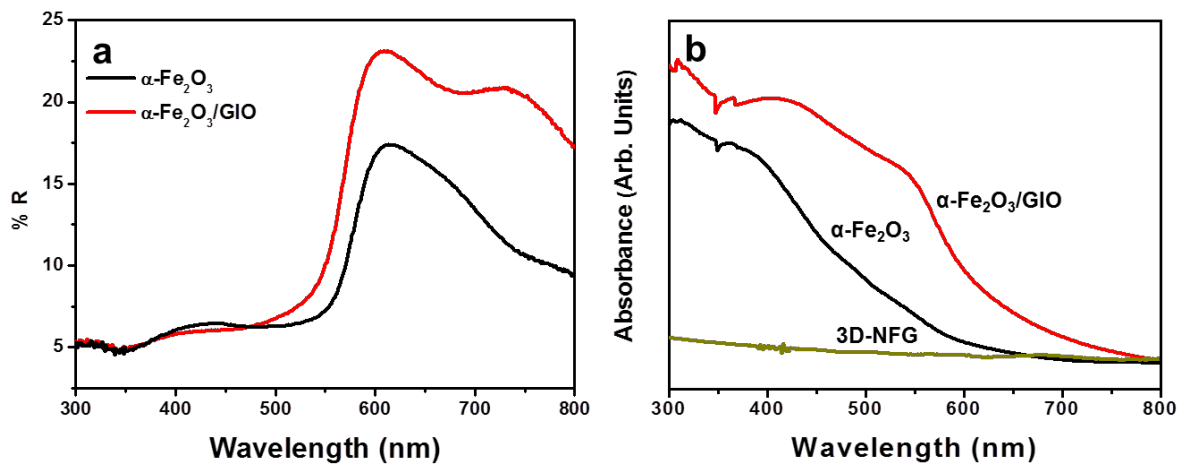


Figure 2.11 Optical properties of $\alpha\text{-Fe}_2\text{O}_3/\text{GIO}$. (a) Diffuse reflectance spectra. (b) UV-visible spectra.

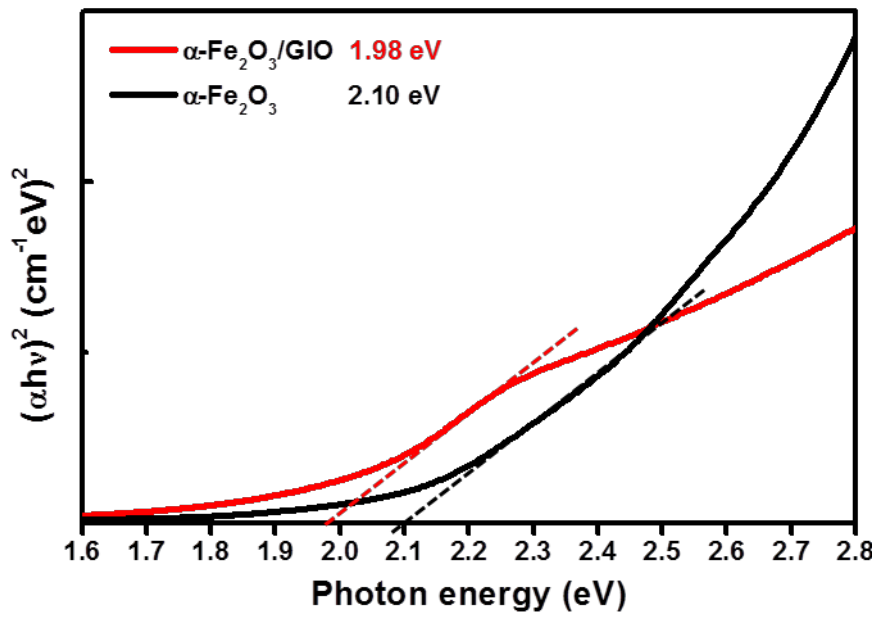


Figure 2.12 Tauc plot for $\alpha\text{-Fe}_2\text{O}_3$ and $\alpha\text{-Fe}_2\text{O}_3/\text{GIO}$

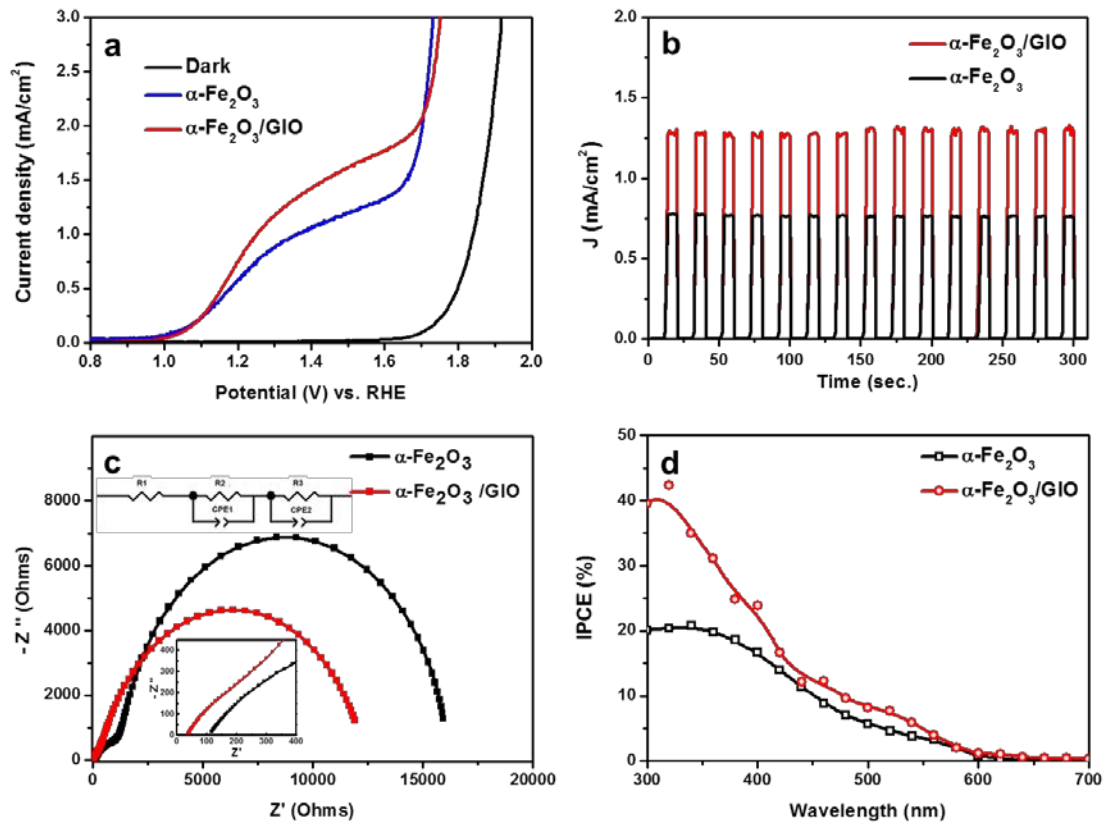


Figure 2.13 Photocurrent behaviors of $\alpha\text{-Fe}_2\text{O}_3/\text{GIO}$. (a) The photocurrent vs. potential of $\alpha\text{-Fe}_2\text{O}_3$ and $\alpha\text{-Fe}_2\text{O}_3/\text{GIO}$ under UV-visible and dark conditions. (b) I-t curve of $\alpha\text{-Fe}_2\text{O}_3/\text{GIO}$ at a bias of 1.5 V vs. RHE under UV-visible light illumination. (c) Nyquist plots and (d) IPCE of $\alpha\text{-Fe}_2\text{O}_3$ and $\alpha\text{-Fe}_2\text{O}_3/\text{GIO}$ at a bias of 0.5 V vs. open circuit potential under illumination.

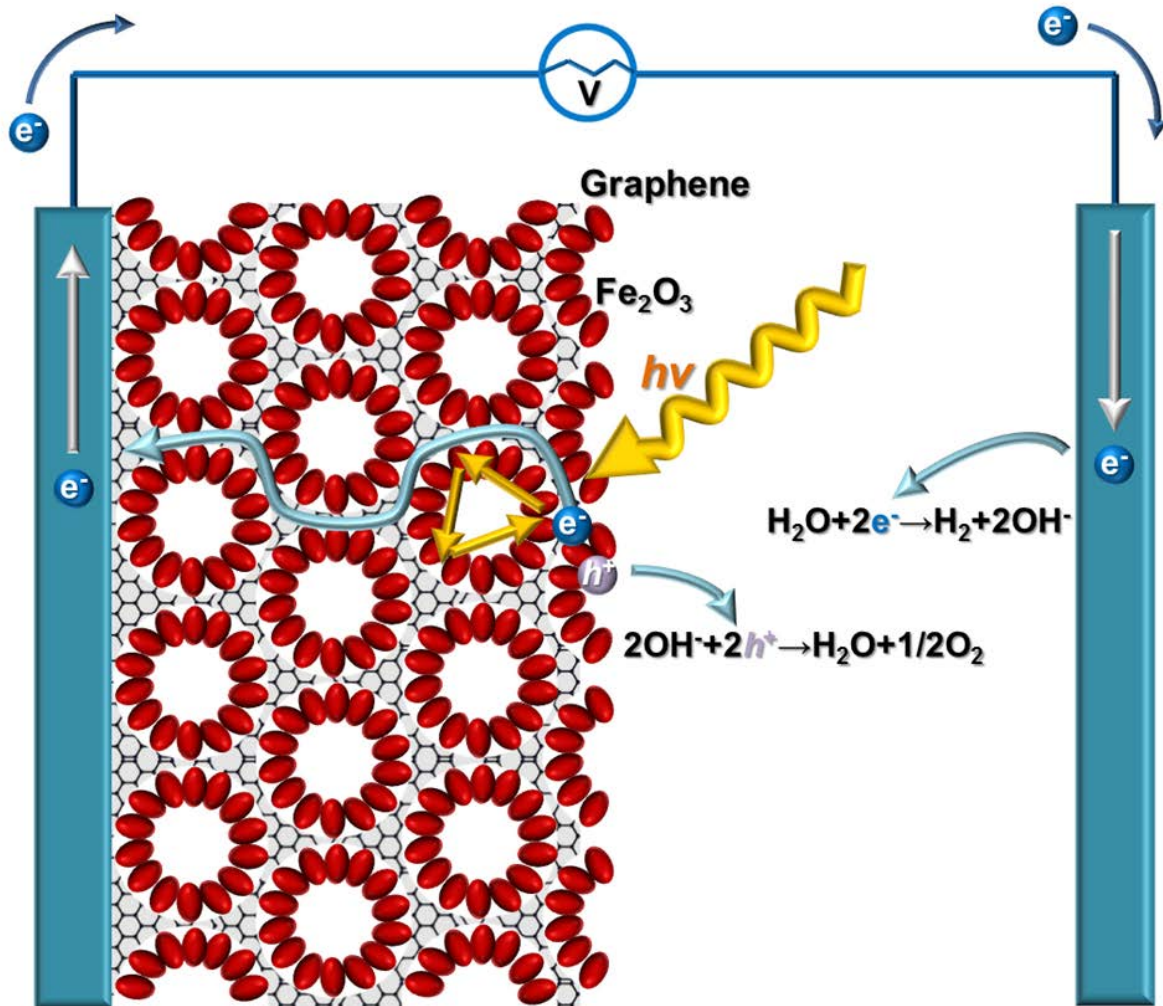


Figure 2.14 Schematic diagram of water splitting of $\alpha\text{-Fe}_2\text{O}_3/\text{GIO}$ with photon trapping effects and direct contact of $\alpha\text{-Fe}_2\text{O}_3$ with the 3D-graphene nano-network conductive electrode.

2.4 Conclusion

In summary, we have presented that by connecting 3D nano-network graphene with photo-anode materials, the low hole diffusion length problem and short absorption in $\alpha\text{-Fe}_2\text{O}_3$ was proficiently handled, and thus the PEC photo-current density made by $\alpha\text{-Fe}_2\text{O}_3$ could be significantly improved. 3D nano-network graphene, directly growing FTO glass at 500°C of low temperature settings, offers the 3D conducting networks graphene for transporting electrons and photon scattering effects. The diffusion reflectance spectrum and EIS analysis separately showed the improved absorption, and fast electron transfer pathways and the existence of straight and reduced electron-hole pair recombination in $\alpha\text{-Fe}_2\text{O}_3$ /GIO displayed 1.4 times higher photo-current value than photo-current value of normal $\alpha\text{-Fe}_2\text{O}_3$ at 1.5 V bias vs RHE. Also, the preparation technique and the procedure for the design presented here can be cheerfully prolonged to other metal oxide systems and material, indicating that offer great potential for our approach in energy- relative systems.

2.5 References

1. Fujishima, A.; Honda, K., Electrochemical Photolysis of Water at a Semiconductor Electrode. *Nature* **1972**, *238*, 37.
2. Walter, M. G.; Warren, E. L.; McKone, J. R.; Boettcher, S. W.; Mi, Q.; Santori, E. A.; Lewis, N. S., Solar Water Splitting Cells. *Chem. Rev.* **2010**, *110*, 6446.
3. Sivula, K.; Le Formal, F.; Gratzel, M., Solar Water Splitting: Progress Using Hematite (α - Fe_2O_3) Photoelectrodes. *ChemSusChem* **2011**, *4*, 432.
4. Kim, J. Y.; Magesh, G.; Youn, D. H.; Jang, J. W.; Kubota, J.; Domen, K.; Lee, J. S., Single-Crystalline, Wormlike Hematite Photoanodes for Efficient Solar Water Splitting. *Sci. Rep.* **2013**, *3*, 2681.
5. Sanchez, C.; Sieber, K. D.; Somorjai, G. A., The Photoelectrochemistry of Niobium Doped Alpha- Fe_2O_3 . *J. Electroanal. Chem.* **1988**, *252*, 269.
6. Wheeler, D. A.; Wang, G.; Ling, Y.; Li, Y.; Zhang, J. Z., Nanostructured Hematite: Synthesis, Characterization, Charge Carrier Dynamics, and Photoelectrochemical Properties. *Energy Environ. Sci.* **2012**, *5*, 6682.
7. Ahn, H.-J.; Kwak, M.-J.; Lee, J.-S.; Yoon, K.-Y.; Jang, J.-H., Nanoporous Hematite Structures to overcome Short Diffusion Lengths in Water Splitting. *J. Mater. Chem. A* **2014**, *2*, 19999.
8. Hou, Y.; Zuo, F.; Dagg, A.; Feng, P., A Three-Dimensional Branched Cobalt-Doped α - Fe_2O_3 Nanorod/ MgFe_2O_4 Heterojunction Array as a Flexible Photoanode for Efficient Photoelectrochemical Water Oxidation. *Angew. Chem. Int. Ed.* **2013**, *52*, 1248.
9. Klahr, B.; Gimenez, S.; Fabregat-Santiago, F.; Bisquert, J.; Hamann, T. W., Photoelectrochemical and Impedance Spectroscopic Investigation of Water Oxidation with "Co-Pi"-Coated Hematite Electrodes. *J. Am. Chem. Soc.* **2012**, *134*, 16693.
10. Tilley, S. D.; Cornuz, M.; Sivula, K.; Gratzel, M., Light-Induced Water Splitting with Hematite: Improved Nanostructure and Iridium Oxide Catalysis. *Angew. Chem. Int. Edit.* **2010**, *49*, 6405.
11. Halaoui, L. I.; Abrams, N. M.; Mallouk, T. E., Increasing the Conversion Efficiency of Dye-Sensitized TiO_2 Photoelectrochemical Cells by Coupling to Photonic Crystals. *J. Phys. Chem. B* **2005**, *109*, 6334.
12. Chen, J. I. L.; von Freymann, G.; Choi, S. Y.; Kitaev, V.; Ozin, G. A., Slow Photons in The Fast Lane in Chemistry. *J. Mater. Chem.* **2008**, *18*, 369.
13. Chen, X.; Ye, J.; Ouyang, S.; Kako, T.; Li, Z.; Zou, Z., Enhanced Incident Photon-to-Electron Conversion Efficiency of Tungsten Trioxide Photoanodes Based on 3D-Photonic Crystal Design. *ACS Nano* **2011**, *5*, 4310.

14. Nishimura, S.; Abrams, N.; Lewis, B. A.; Halaoui, L. I.; Mallouk, T. E.; Benkstein, K. D.; van de Lagemaat, J.; Frank, A. J., Standing Wave Enhancement of Red Absorbance and Photocurrent in Dye-Sensitized Titanium Dioxide Photoelectrodes Coupled to Photonic Crystals. *J. Am. Chem. Soc.* **2003**, *125*, 6306.
15. Zhang, H.; Lv, X. J.; Li, Y. M.; Wang, Y.; Li, J. H., P25-Graphene Composite as a High Performance Photocatalyst. *ACS Nano* **2010**, *4*, 380-386.
16. Xiang, Q. J.; Yu, J. G.; Jaroniec, M., Synergetic Effect of MoS₂ and Graphene as Cocatalysts for Enhanced Photocatalytic H₂ Production Activity of TiO₂ Nanoparticles. *J. Am. Chem. Soc.* **2012**, *134*, 6575.
17. Yoon, S.-M.; Choi, W. M.; Baik, H.; Shin, H.-J.; Song, I.; Kwon, M.-S.; Bae, J. J.; Kim, H.; Lee, Y. H.; Choi, J.-Y., Synthesis of Multilayer Graphene Balls by Carbon Segregation from Nickel Nanoparticles. *ACS Nano* **2012**, *6*, 6803.
18. Lee, J.-S.; Ahn, H.-J.; Yoon, J.-C.; Jang, J.-H., Three-Dimensional Nano-Foam of Few-Layer Graphene Grown by CVD for DSSC. *Phys. Chem. Chem. Phys.* **2012**, *14*, 7938.

Chapter 3. Graphene Quantum-Dot Protected Cadmium Selenide Quantum-Dot Sensitized Photoanode for Efficient Photo-electrochemical Cells with Enhanced Stability and Performance

3.1 Introduction

Photoelectrochemical (PEC) cells have been an attractive research area for efficient hydrogen generation for several decades. Among the various photoanode materials for PEC systems,¹⁻² TiO₂ is one of the most promising due to its low cost and its environmentally friendly and long-term stable properties.³ However, the non-visible light responsivity of pure TiO₂ due to its large band gap (about 3.2V) restricts further improvement of solar energy conversion efficiency. To overcome this limitation, many strategies have been applied to TiO₂ photoanodes, such as nanostructuring,⁴ doping with metal or nonmetal elements,⁵⁻⁸ coupling with secondary semiconductors, and photosensitization of dyes.⁹⁻¹¹ For example, the coupling of TiO₂ with quantum dots such as CdSe,¹² CdS,¹³ and PbS¹⁴ has achieved some success in broadening the absorption spectrum to the visible and near infrared region, thereby greatly enhancing the solar-to-hydrogen efficiency of PEC cells. However, cadmium chalcogenide quantum dots are often unstable in water under irradiation of light due to their relatively slower interfacial hole transfer kinetics as compared to their electron injection rates.¹⁵⁻¹⁶ In order for cadmium chalcogenide quantum dots to be broadly used for PEC systems, it is crucial to address the instability problem by improving hole transfer kinetics.

Iridium oxide (IrO₂) has recently been studied more intensively as an oxygen evolution catalyst with the ability of increasing the stability of photoanodes.¹⁷⁻¹⁸ Yong's et al. demonstrated that CdSe/CdS co-sensitized ZnO decorated with IrO₂ exhibited a long-term stability of about 95% retention after 3hrs.¹⁷ The successive hole scavenging by IrO₂ greatly retarded electron-hole recombination. However, iridium is a rare earth element and very expensive. An efficient solution to the problem of photochemical stability thus remains a significant challenge.

Graphene quantum dots (GQDs) have shown good performance including chemical stability, non-toxicity, high carrier transport mobility, and large-scale production capability with low cost as well as a unique strong and size-dependent photoluminescence (PL) emission.¹⁹⁻²¹ On this basis, GQDs have been successfully utilized in sensors,²² light-emitting devices,²³ and bio-imaging.²⁴ In addition, GQDs were shown to be both excellent electron donors and extractor. The conjugated π structure of GQDs plays an important role in their improved photocatalytic activities by facilitating the adsorption of organic dyes.²⁵⁻²⁷ For example, Titirici et al. reported on a carbon@TiO₂ dyade structure with improved TiO₂ hole reactivity and photocatalytic properties.²⁷ Herein, we report that GQDs can be used as an inexpensive and efficient hole accepting catalyst to improve the stability of CdSe-sensitized PEC systems. The ability of GQDs to serve simultaneously as a good electron donor and a

hole extractor was confirmed by the fast PL decay and a photodegradation experiment in GQDs/CdSe/P25, respectively. Our results confirmed that GQDs can increase the stability as well as enhance the photo-response of the CdSe/P25 photoanode in the UV-vis range.

3.2 Experimental Procedures

3.2.1 Synthesis of GQDs

In order to synthesize GQDs, pitch carbon fiber (0.3g) was added into a mixture of H_2SO_4 (60mL) and HNO_3 (20mL).²¹ The solution was sonicated for two hours and stirred for 24 hours at 100 °C. The size of the GQDs was controlled by the reaction temperature (80 °C-140 °C). The mixture was cooled and diluted with deionized (DI) water (800mL). The pH was adjusted to 8 with Na_2CO_3 . The product solution was then dialyzed in a dialysis bag with a molecular weight cut-off of 2000 Dalton for one week. The final GQDs solution with the concentration of 2.6 mg/mL was used for deposition without further purification.

3.2.2 Preparation of GQDs/CdSe/P25 photoanode

A densely packed P25 photoanode was fabricated on FTO glass by doctor blade coating. To ensure good contact between P25 and the substrate, O_2 plasma treated FTO glass was dip-coated in a 40 mM TiCl_4 aqueous solution followed by annealing at 70°C for 30 minutes. Scotch tape was applied to make a window with a working area of 5mm X 5mm. Samples were annealed at 120 °C for 10 minutes and 550 °C for 1 hr. A typical successive ionic layer adsorption and reaction (SILAR) was carried out to deposit CdSe onto P25. A sodium selenosulfate (Na_2SeSO_3) solution was prepared by dissolving 0.01 mol Se powder in a 0.1 M Na_2SO_3 solution at 90 °C for 9 hrs. Then, the P25 substrate was dipped into a 50 mM $\text{Cd}(\text{Ac})_2 \cdot 2\text{H}_2\text{O}$ absolute ethanol for 1 min, rinsed with absolute ethanol for 30 s, dipped into a Na_2SeSO_3 solution for 1 min, and washed with D.I. water for 30 s. Finally, the CdSe/P25 substrate was dried by blowing nitrogen gas. The two-step dipping procedure is designated as a one SILAR cycle, and a fifteen times SILAR cycle was applied to obtain optimized CdSe concentration. All steps were carried out in a nitrogen gas-filled glove box. Then CdSe/P25 on FTO glass was immersed into GQDs solutions for various times of 1, 2, 3 hrs in a dark condition. They were subsequently taken out, rinsed with DI water, and dried at 70°C overnight.

3.2.3 Photo-electrochemical measurement

The PEC performance of CdSe/P25 and GQDs/CdSe/P25 electrodes was explored in a three-cell electrode system under front-side illumination of AM 1.5G. An Ag/AgCl electrode and a Pt mesh were used as a reference and a counter electrode, respectively. A solution of Na₂S/Na₂SO₃ was used as an electrolyte. Photocurrent stability tests were carried out by measuring the photocurrent produced under chopped light irradiation (light/dark cycles of 30s) at a bias of 0.3 V vs Ag/AgCl. Electrochemical impedance spectroscopy (EIS) was carried out at a frequency range from 100 kHz to 0.1 Hz using a potentiostat. The incident photon to current conversion efficiency (IPCE) was measured under monochromatic light by a Xe lamp providing illumination through a monochromator. The illumination intensity of the monochromatic light was measured by a luminometer.

3.3 Results and Discussion

The energy levels of three different active materials in GQDs/CdSe/P25 systems are shown in Fig. 3.1a (see Figure 3.2 for details of the alignment of the energy level).²⁸ The proper band energy values would produce significant synergy for efficient transport of photoexcited electrons and holes in the electrode. Because cadmium chalcogenide quantum dots have relatively slower interfacial hole transfer kinetics compared to the electron injection rate into TiO₂, the holes gradually accumulate within quantum dots and promote hole-induced anodic corrosion. Therefore, reduction of the photocurrent over time is an inevitable problem in this system. To overcome this problem, we decorated the surface of CdSe with a good hole extractor, GQDs, which could considerably improve the stability as well as the photocatalytic activity of the photoelectrode. Upon light excitation, electrons are excited from the valence band (VB) to the conduction band (CB) of TiO₂, CdSe, and GQDs. The photoexcited electrons at the conduction band of P25 transferred from GQDs/CdSe quantum dots by the stepwise energy level are collected on FTO and move to the Pt counter electrode via the external circuit and generate hydrogen. On the other hand, the photoexcited holes in the CdSe/P25 electrode rapidly converge at the surface of GQDs and are then scavenged by polysulfide redox couples, which helps reduce the corrosion of CdSe/P25. The polysulfide (0.24 M Na₂S and 0.35 M Na₂SO₃) redox couples (S²⁻/S_n²⁻) were used in scavenging the holes of CdSe quantum dots to maintain the stability of the system. Figure 3.1b shows the fabrication process for the GQDs/CdSe/P25 system. First, CdSe quantum dots were deposited on a P25/FTO electrode with a final thickness of 8 μm, by the doctor blade method. A typical successive ionic layer adsorption and reaction (SILAR) was carried out and was repeated fifteen times to obtain optimized CdSe deposition. The CdSe/P25 substrate was then immersed in a GQDs solution for 1h to adsorb the GQDs. The sample was thoroughly washed with DI water and dried at 70 °C overnight.

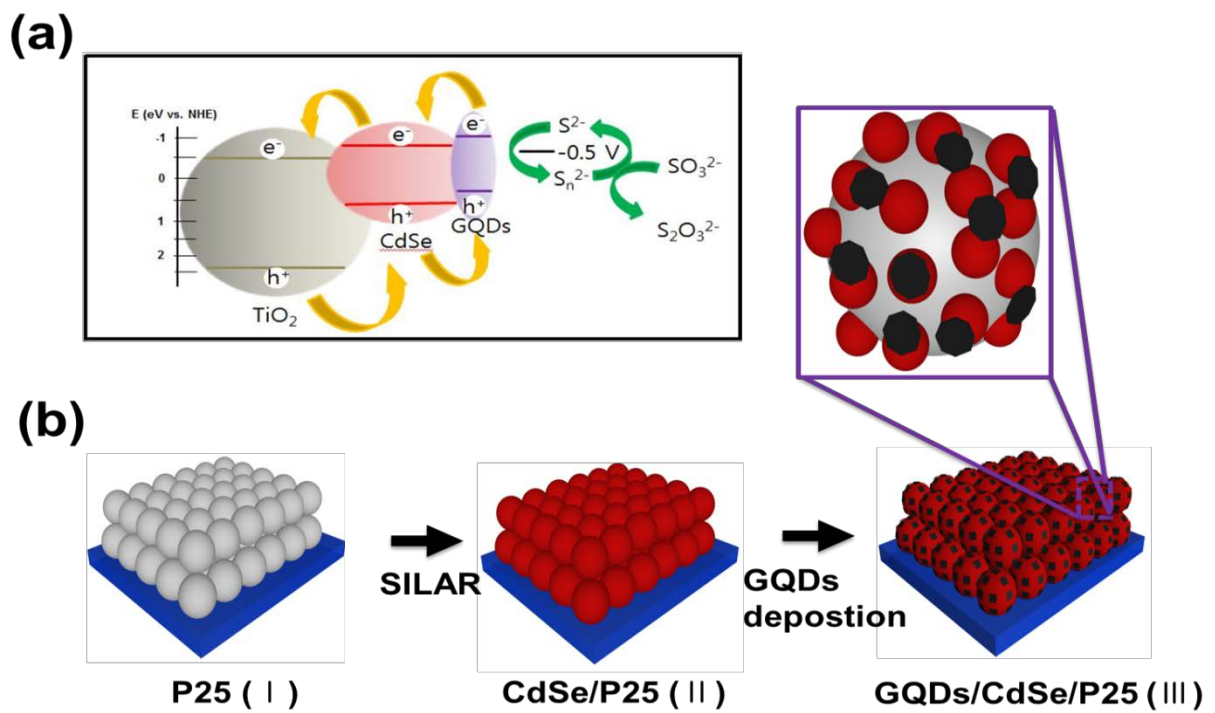


Figure 3.1 Schematic illustration of (a) the proposed band diagram and (b) the fabrication procedure for GQDs/CdSe/P25. P25 (I), CdSe/P25 (II), and GQDs/CdSe/P25 (III).

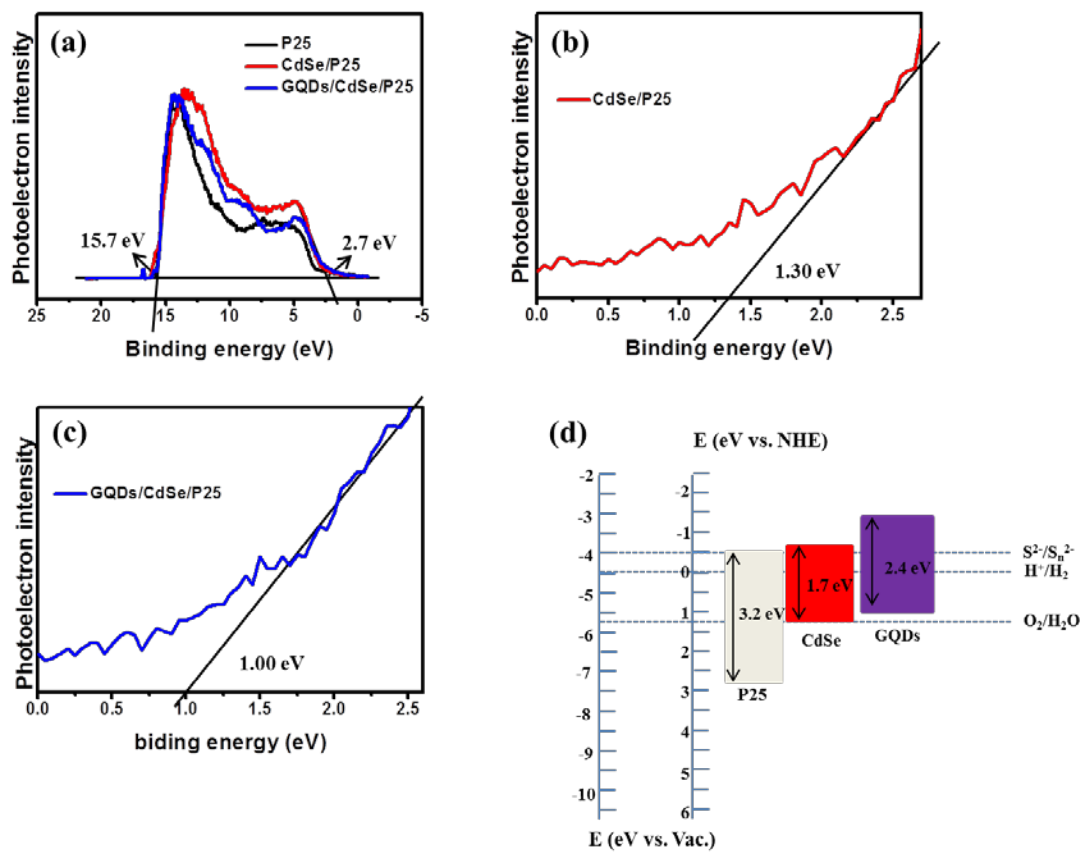


Figure 3.2 UPS data for band gap alignment. (a) Full spectra of UPS for the valence band position and band energy of GQDs/CdSe/P25. (b) UPS for CdSe/P25 and (c) GQDs for valence band position. (d) The energy diagram.

Before we investigated the effects of GQDs in the GQDs/CdSe/P25 PEC system, we assessed the properties of synthesized GQDs. Figure 3.3a shows the UV-VIS absorption spectrum of GQDs with a wide and strong absorption band in the ultraviolet and visible region. The challenge of harvesting energy in a wide range of light covering the visible range has been studied over many years in areas where sunlight is used as an energy source.²⁹⁻³⁰ In this context, GQDs with a broad spectral absorption range have an advantage in application as a photosensitizer. Figure 3.3b exhibits excitation-dependent photoluminescence (PL) spectra of GQDs. The spectra indicate that the photoexcited charge carriers can be generated by a broad range of UV and visible light. The transmission electron microscopy (TEM) image in Figure 3.3c shows GQDs with an average size of 5.6 nm with a narrow size distribution. The HR-TEM image in the inset of Figure 3.3c denotes lattice spacing of about 0.24nm, corresponding to the (1120) plane of a honeycomb lattice of graphitic carbon, indicating high crystallinity of GQDs.²¹ Typical C1s peaks of GQDs were detected in the XPS spectrum in Figure 3.3d. Three peaks corresponding to C-C, C-OH/C-O-C, C=O and COOH at 284.46, 285.95, 287.5 and 288.38 eV, respectively, confirm the successful creation of GQDs.³¹⁻³² To demonstrate the successful loading of the GQDs on the CdSe/P25 electrodes, we carried out electron microscopy and time-resolved photoluminescence (PL) decay measurements for CdSe/P25 and GQDs/CdSe/P25. The TEM and HRTEM images in Figures 3.4a and 3.4b present GQDs/CdSe/P25 composites with close contact of the GQDs on CdSe/P25. The lattice spacing of 0.24 nm, 0.165 nm, and 0.34 nm, corresponding to the (1120) plane of GQDs, the (202) plane of CdSe, and the (101) plane of P25, respectively, in the HRTEM image (Figure 3.3b) reflects tight and stepwise deposition of CdSe and GQDs on the surface of P25.^{10, 21, 33} As shown in XPS data (Figure 3.5), the C1s peak of GQDs/CdSe/P25 is well matched with C1s peak in Figure 3.3d. In addition, we identified uniform dispersion of Ti, O, Cd, Se, and C elements over the samples, as shown in Figure 3.6. Further analyses (Raman, FT-IR and XRD) to confirm the presence of GQDs on CdSe/P25 are presented in Figure 3.6 and Figure 3.7. Seen from the Raman spectra, four distinct peaks centered at 146 cm⁻¹, 396 cm⁻¹, 519 cm⁻¹, 639 cm⁻¹ can be ascribed to characteristic Raman active modes of pristine anatase TiO₂ according to the symmetry group analysis. Three additional D-band, G-band, and 2D-band peaks centered at 1336 cm⁻¹, 1547 cm⁻¹, and 2670 cm⁻¹, respectively, of GQDs should be observed in the spectrum for GQDs/CdSe/P25. However, GQDs peaks in GQDs/CdSe/P25 were obscured due to the fluorescence peaks of GQDs and CdSe. Alternatively, the FT-IR spectra showed the most prominent GQDs peaks of C=C at 1600 cm⁻¹ and that of C-O at 1138 cm⁻¹. The results confirmed that the GQDs were deposited on the surface of CdSe. The typical graphene peak for GQDs at 26° corresponding to the (002) plane was not detected because the peaks of FTO and CdSe overlapped with the peak of carbon. Figure 3.4c compares time-resolved PL decay profiles of CdSe/P25 and GQDs/CdSe/P25 at 470 nm. The average decay lifetime of GQDs/CdSe/P25 is clearly shorter than that of CdSe/P25, indicating fast transfer of photoexcited

electrons as shown in Figure 3.8. This proves that GQDs act as good electron donors, as explained in the energy level diagram in Figure 3.1a, implying that properly positioned GQDs are promising sensitizers for enhancing the photo-response of CdSe/P25.

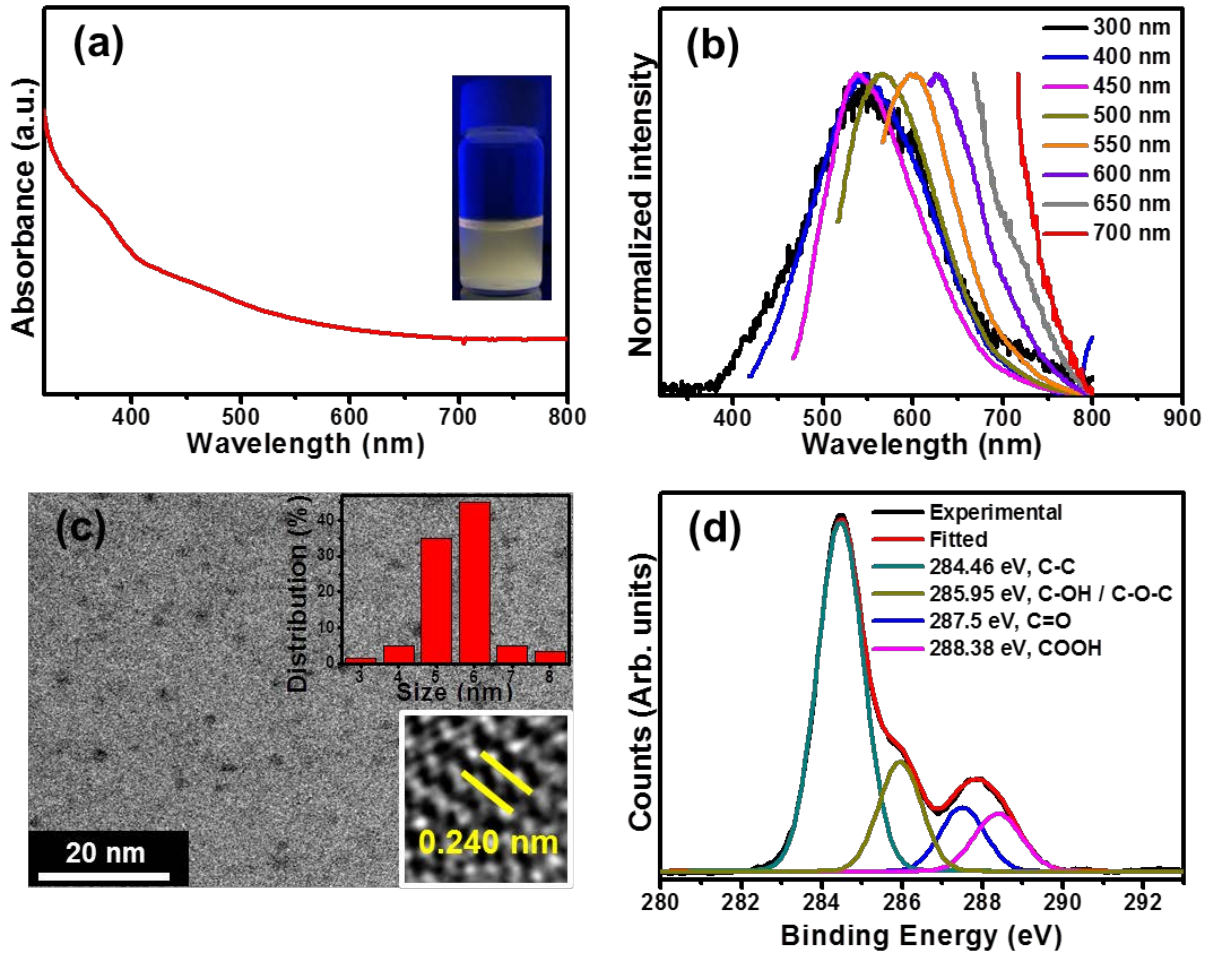


Figure 3.3 Characterization of GQDs: (a) UV-VIS absorption spectrum of GQDs. (b) Normalized PL spectra of the GQDs with different excitation wavelengths. (c) TEM and HR TEM images. (d) XPS spectra

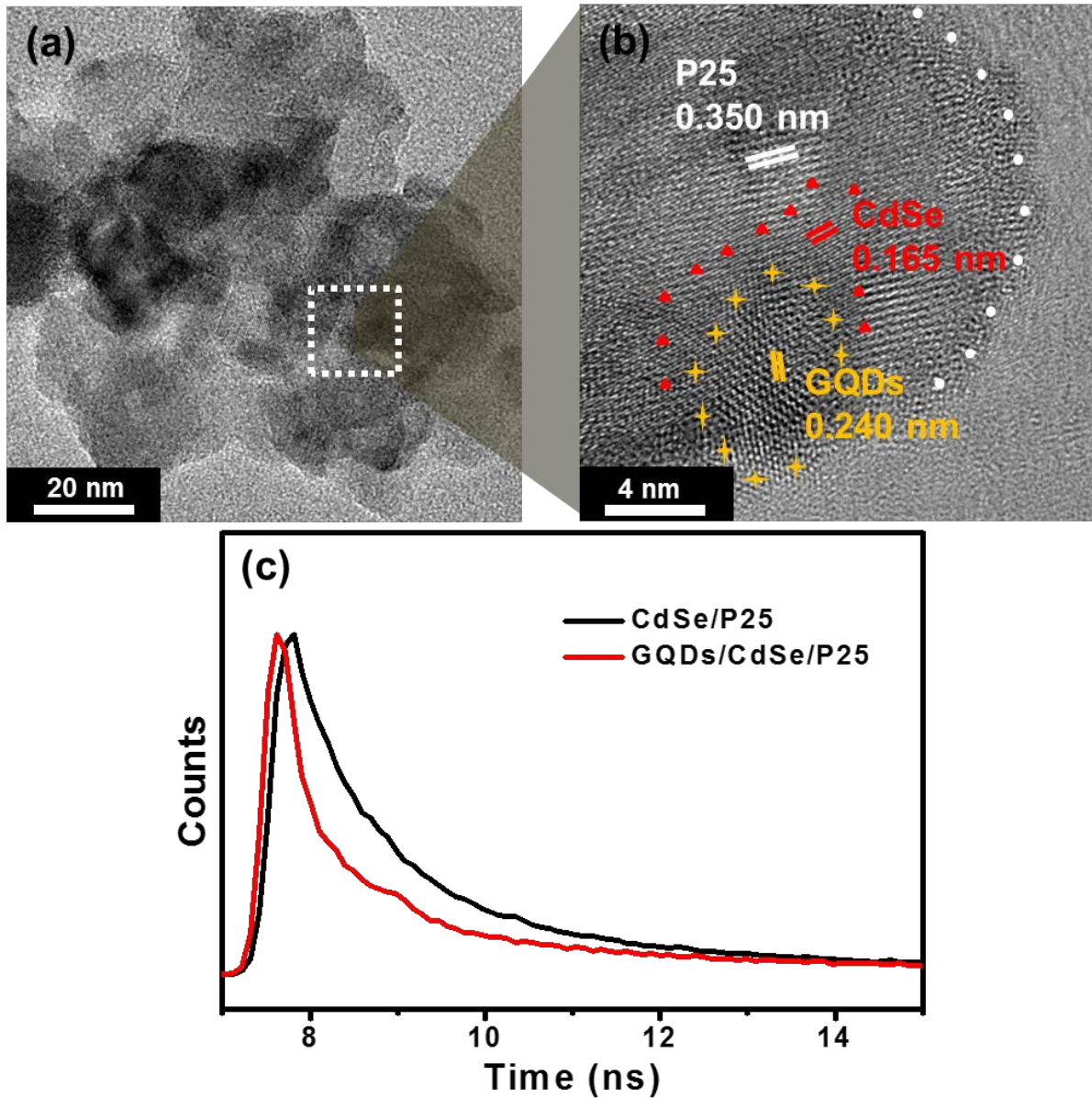


Figure 3.4 (a) TEM images of GQDs/Cdse/P25. (b) Zoomed-up images of the highlighted region in (a). (c) Time-resolved PL decay profiles of CdSe/P25 and GQDs/CdSe/P25.

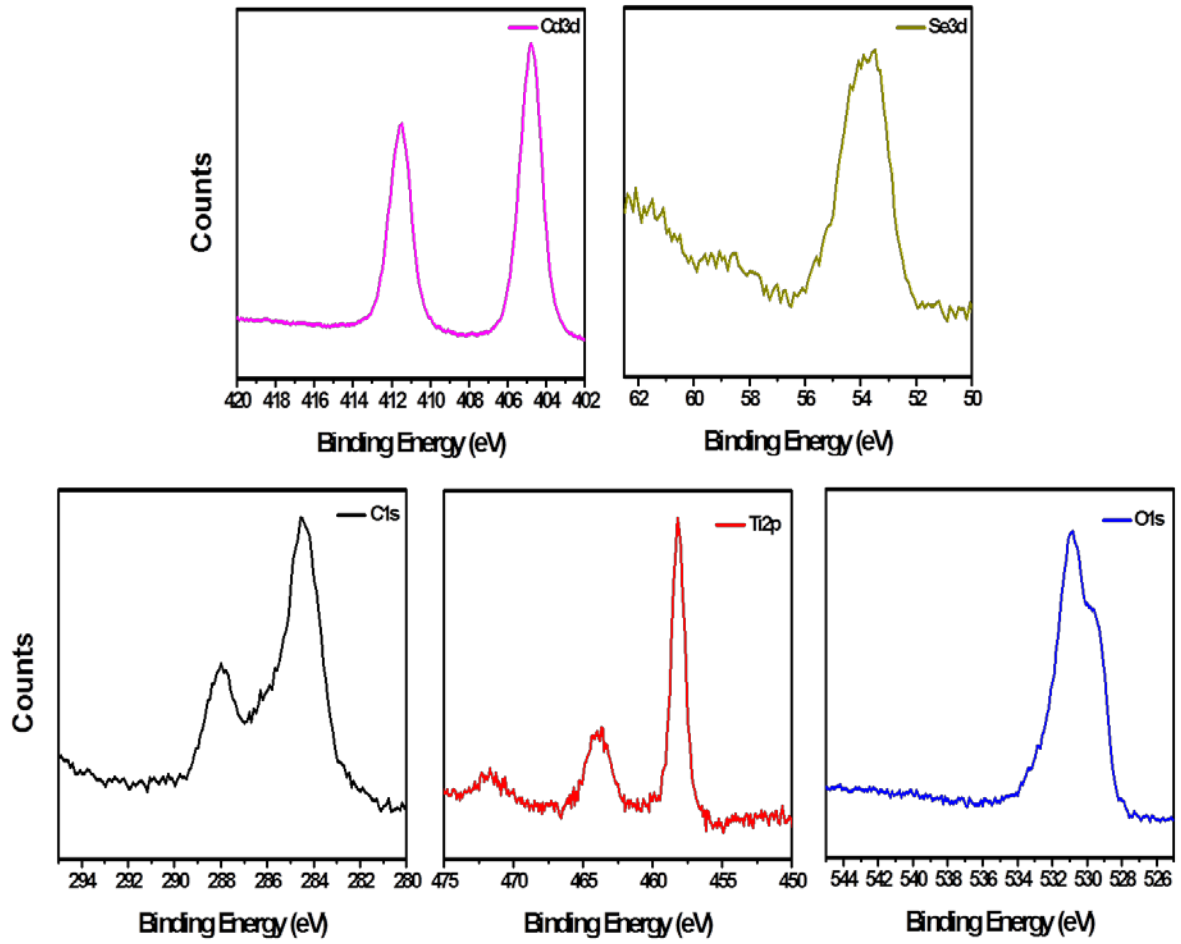


Figure 3.5 XPS analysis of GQDs/CdSe/P25.

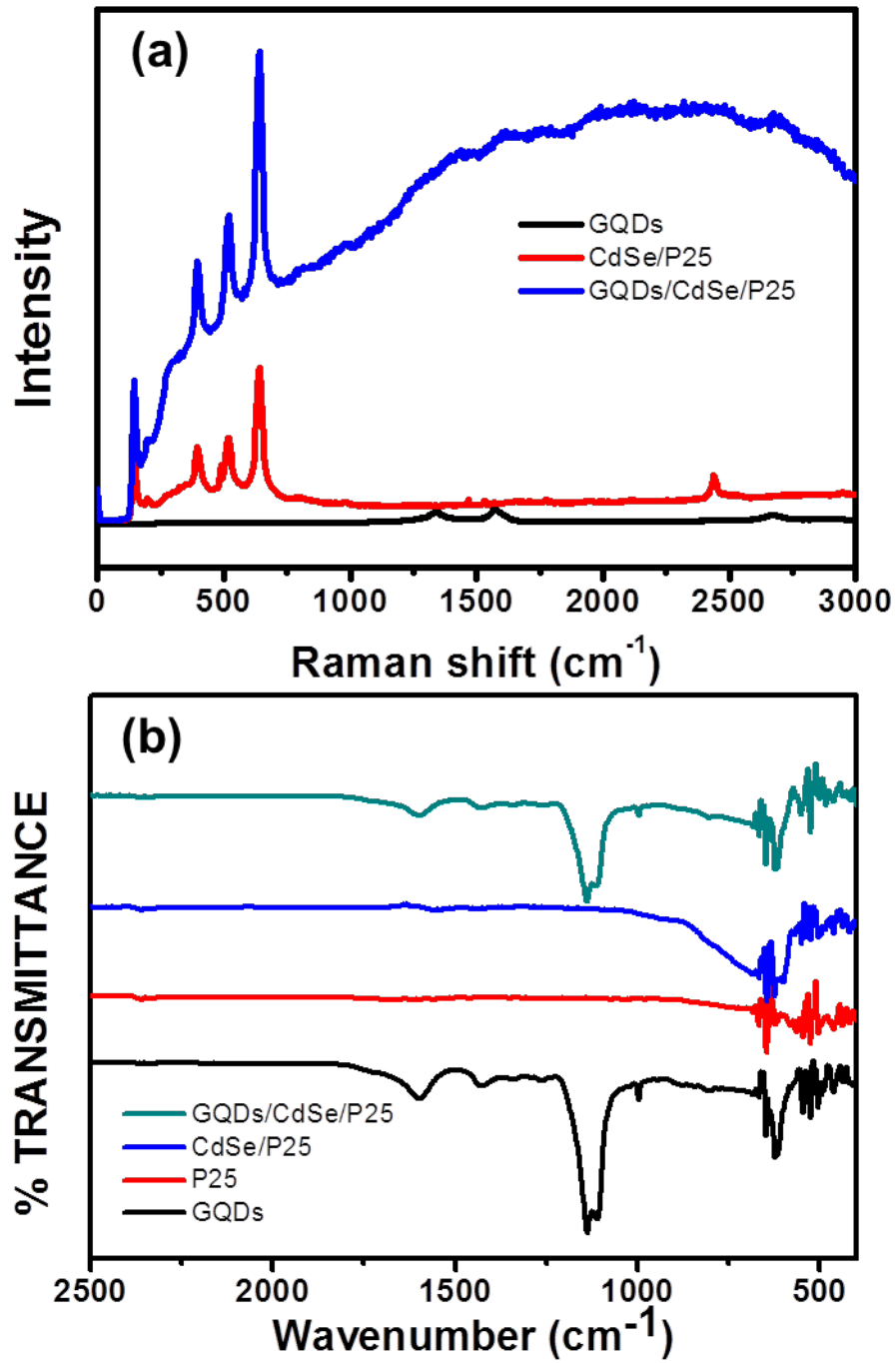


Figure 3.6 (a) Raman spectra and (b) FT-IR spectrum.

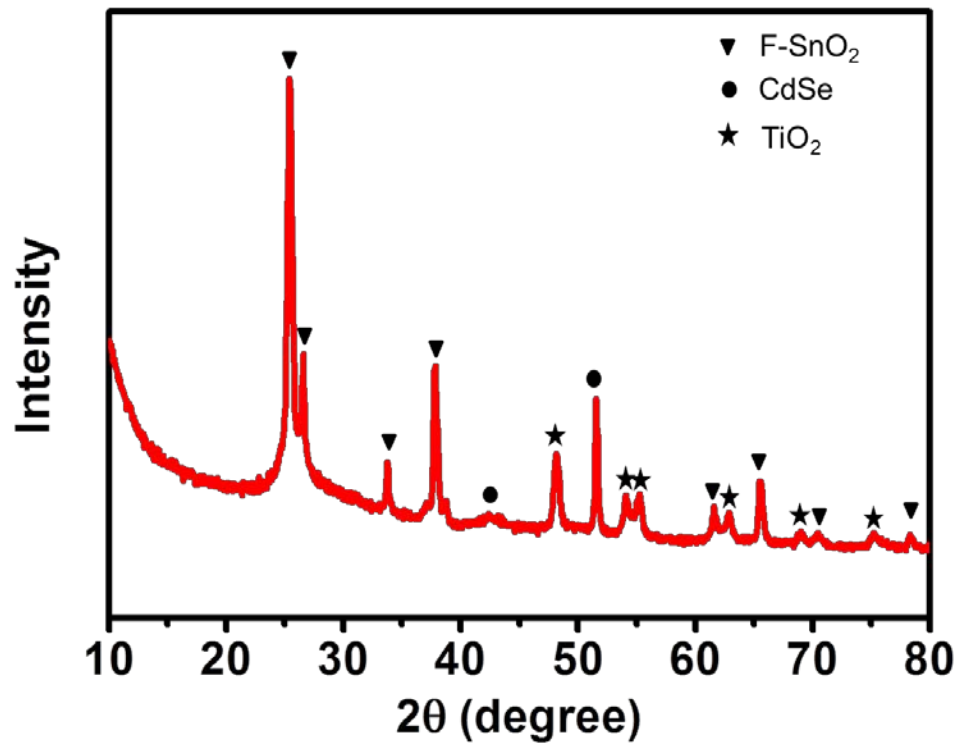


Figure 3.7 XRD analysis of GQDs/CdSe/P25.

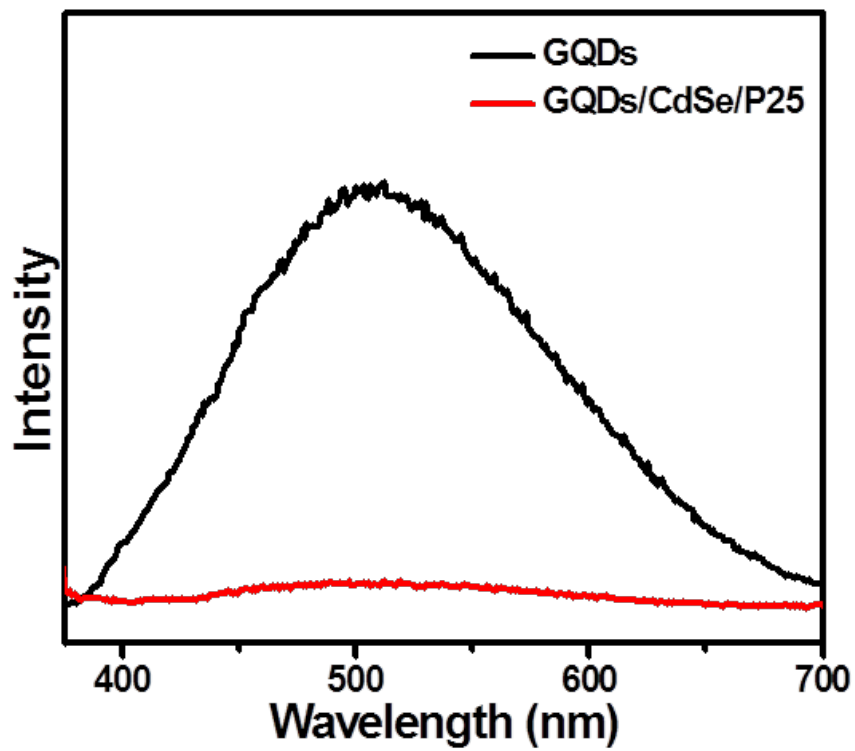


Figure 3.8 Photoluminescence (PL) spectra of GQDs and GQDs/CdSe/P25.

Figure 3.9 compares the PEC performance of CdSe/P25 w/wo GQDs as a PEC electrode. We optimized the performance of the GQDs/CdSe/P25 photoanode by controlling the deposition time of the GQDs on CdSe/P25, as shown in Figure 3.10. When the GQD loading time was longer than 1h, the photocurrent density of GQDs/CdSe/P25 decreased gradually. The photocurrent depression could be attributed to two possible reasons. First, a large number of GQDs at the longer deposition time may result in a large portion of GQDs locating on the surface of CdSe/P25, which retards the access of UV light to the other active materials, P25 and CdSe. Second, such a high coverage of GQDs may reduce the number of reactive sites of CdSe/P25 for the contact of holes with the electrolyte, and thereby hinders the photocatalytic reactions. The light absorption spectra of P25, CdSe/P25, and GQDs/CdSe/P25 are shown in Figure 3.9a. CdSe/P25 showed a broadened absorption spectrum in the visible range compared to P25 due to the visible light excitation behavior of CdSe. Enhanced absorption in the UV-vis range, which is advantageous for photosensitization of a PEC system, was observed in GQDs/CdSe/P25 as compared to CdSe/P25. Figure 3.9b presents the photocurrent density (J)-potential (V) curves at a scan rate of 20 mV/s with front side illumination of one sun AM1.5G. The photocurrent density of GQDs/CdSe/P25 reached 14.16 mA/cm² at an applied bias of 0.3 V. This is approximately 20% greater than that of the optimized CdSe/P25 (12.03 mA/cm²). The enhancement in the photocurrent density of GQDs/CdSe/P25 suggests that the GQDs were effective photosensitizers in the CdSe/P25 electrode. When we performed identical experiments with only visible light illumination using a UV-cutoff filter (>420 nm), the photocurrent density of GQDs/CdSe/P25 reached 13.23 mA/cm². Surprisingly, this is a 10% higher value compared to that of CdSe/P25 irradiated with UV-vis light. Therefore, GQDs are a good photosensitizer in the visible range as well as in the UV range as shown in Figure 3.11.

EIS is a powerful tool to explore the electric properties of semiconductor materials and has been widely employed in PEC systems. We obtained EIS curves at a frequency range from 100 kHz to 0.1 Hz with Ag/AgCl potential of 0.6 V under AM 1.5G in 0.24 M Na₂S and 0.35 M Na₂SO₃ electrolytes (pH=12). Figure 3.9c shows the Nyquist plots with an equivalent circuit and fitted experimental values are presented in Table 3.1. R_{Ct}, the charge transfer resistance between the electrolyte/materials, is reflected by the diameter of the semicircles in the low frequency of the Nyquist plot and is associated with the charge transfer kinetics across the interface. The R_{Ct} value of GQD/CdSe/P25 was much lower than that of CdSe/P25, which can be attributed to the improved photocatalytic property and fast hole extraction through GQDs. As described in Table 3.1, the GQDs/CdSe/P25 showed lower recombination resistance inside the bulk material (R_{REC}), reflecting internal resistance. Although the internal resistance of P25 is expected to be similar, the recombination in CdSe is reduced by fast hole transfer to the GQDs, and P25 accepts more charges through GQDs/CdSe, resulting in smaller internal resistance of P25 and increased photocurrent density. The EIS results imply suppressed

recombination and fast charge transfer between the electrolyte and the GQDs in the GQDs/CdSe/P25 system.³⁴⁻³⁵ To further evaluate the PEC properties of GQDs/CdSe/P25, IPCE spectra were measured at 0.3 V vs Ag/AgCl under monochromatic light. As shown in Figure 3.9d, the photo-response of GQD/CdSe/P25 exhibited a 72% IPCE value at a wavelength of 480 nm whereas CdSe/P25 showed a value of 63% at the same wavelength. It is evident that the IPCE value of GQDs/CdSe/P25 was enhanced in the entire UV-vis range of 300-800 nm, consistent with the UV-vis absorption, indicating that the incorporation of GQDs further improved the photo-response of the CdSe sensitized TiO₂ PEC cell in the UV-vis range.

To confirm the enhanced stability of GQDs/CdSe/P25, time-dependent photocurrent measurements have been carried out on CdSe-sensitized photoanodes, as shown in Figure 3.12. The photocurrent density of CdSe/P25 continuously decreased with an increase of time, as shown in Figure 3.12a. The inset image clearly demonstrates the poor stability of CdSe-sensitized TiO₂ for longer exposure time. The photocurrent density of CdSe/P25 decreased to 4.5 mA/cm², a 63% reduction of the initial value, after 100 min. On the contrary, no noticeable decay of the photocurrent density was detected for GQDs/CdSe/P25 during 300 minutes, indicating that the GQDs contributed to enhanced stability of the CdSe-sensitized P25. The higher stability of the GQDs supported photoanode can be explained by the different shape of the J-T curve over time for CdSe/P25 (Figure 3.12a) and GQDs/CdSe/P25 (Figure 3.12b). The J-T curve of CdSe/P25 exhibited a gradually increasing feature during the period of exposure due to the accumulation of holes within quantum dots. This implies that the photoexcited holes on the surface of CdSe have relatively slower interfacial transfer kinetics and thus promote hole-induced anodic corrosion. However, GQDs/CdSe/P25 exhibited relative steady current generation with a sharp increase at the beginning of each exposure, implying fast hole transfer kinetics between the surface and the electrolyte after adopting a good hole extractor, GQDs in CdSe/P25.³⁶ The improved stability of GQDs/CdSe/P25 can be further explained by the properly positioned energy level of GQDs between CdSe and S²⁻/S_n²⁻, which provides fast and easy hole transfer pathways in GQDs/CdSe/P25, compared to CdSe/P25 where a substantial energy difference for hole transfer exists (Figure 3.12c). This can be verified by the change in color of the samples after the measurements. The DC (digital camera) image in Figure 3.13 presents a similar dark red color for CdSe/P25 and GQDs/CdSe/P25 before the measurements. However, after the measurement, a much darker edge of CdSe/P25 was observed due to the corrosion of the electrode from the edge, whereas the color of GQDs/CdSe/P25 remained the same after the measurement.

To further confirm the enhanced properties of GQDs as a hole extractor, we evaluated the photodegradation of methylene blue dyes with CdSe/P25 and GQDs/CdSe/P25, as shown in Figure 3.14. Since photodegradation of methylene blue is caused by the reaction of photoexcited holes of the photoanode,³⁷ we can predict the photocatalytic activity of the samples by measuring the absorbance

of methylene blue. After each sample (CdSe/P25 and GQDs/CdSe/P25) and a methylene blue (50 mg/L) dye solution were irradiated for a given exposure period, the absorbance change was checked by a UV-visible spectrophotometer. The photocatalytic activity of GQDs/CdSe/P25 was 11% higher than that of CdSe/P25 at a time of 60 min, confirming the positive role of GQDs as a hole extractor.

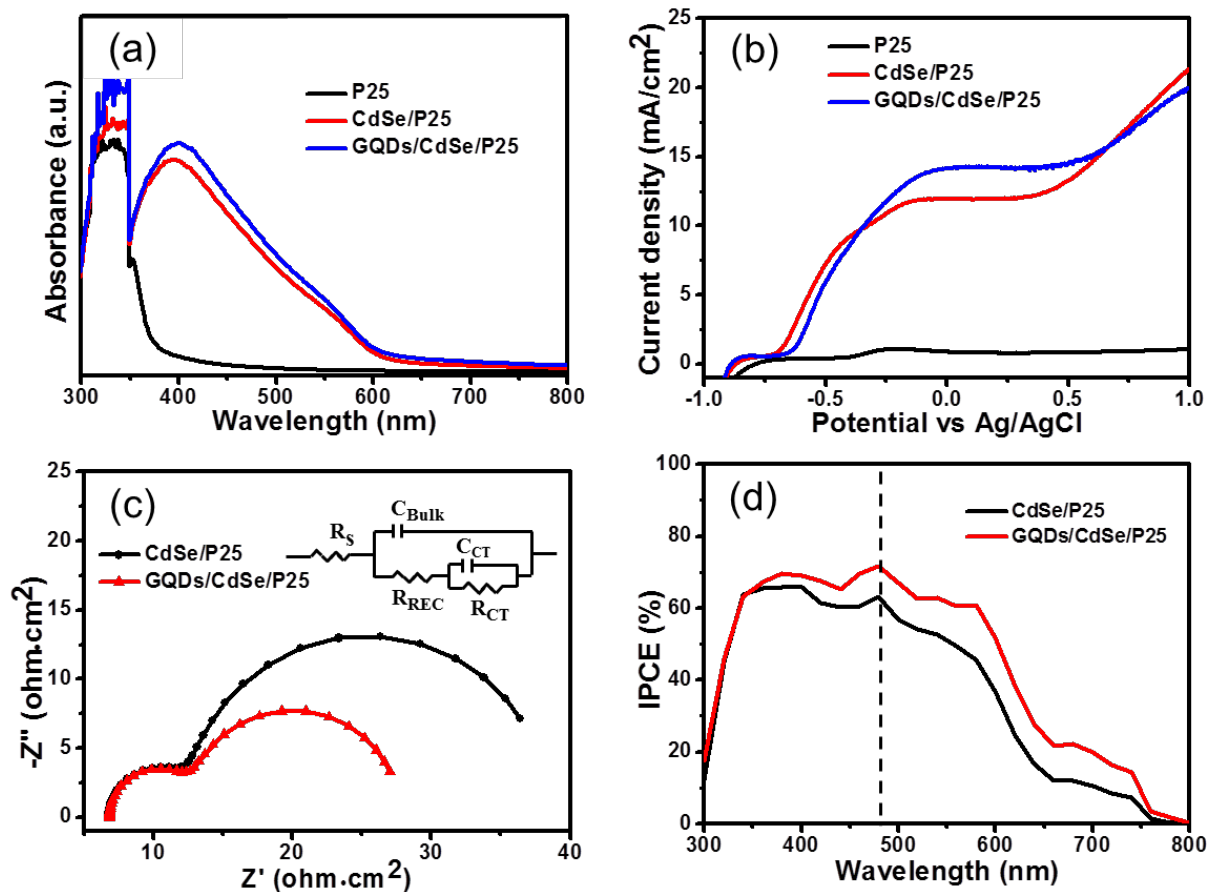


Figure 3.9 (a) UV-VIS absorption spectra of the GQD, P25, CdSe/P25 and GQDs/CdSe/P25 photoanodes. (b) Linear sweep voltammetric (J-V) curves of the three kinds of photoanodes under simulated sunlight illumination. (c) Impedance spectroscopy of CdSe/P25 and GQDs/CdSe/P25. (d) A comparison of the IPCE spectra of the two photoanodes measured at 0.3 V vs Ag/AgCl.

(R / Ω cm²)	R_s	R_{REC}	R_{CT}
CdSe/P25	6.798	7.1	24.63
GQDs/CdSe/P25	6.696	6.2	13.95

Table 3.1 EIS responses of CdSe/P25 and GQDs/CdSe/P25

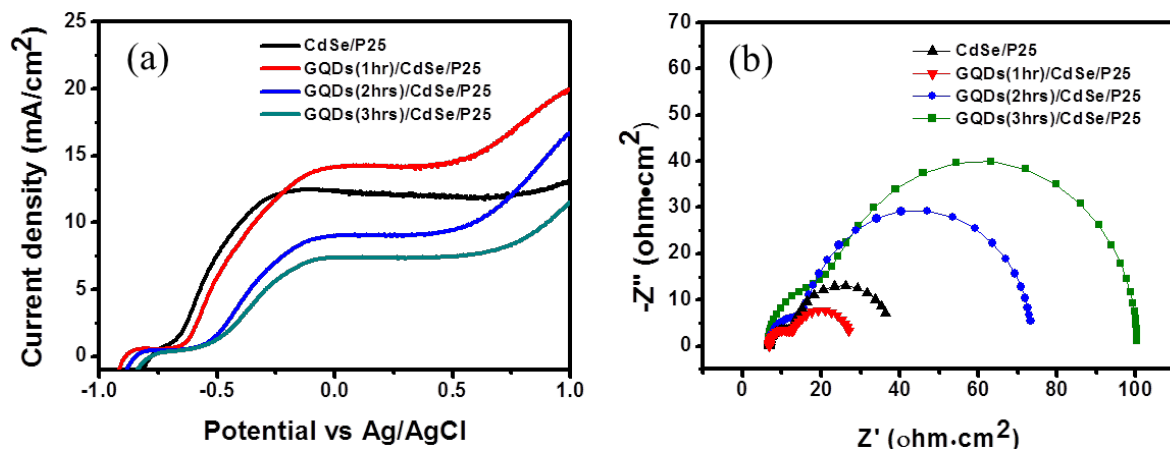


Figure 3.10 (a) J-V curve and (b) EIS for GQDs/CdSe/P25 with different GQD dipping time of 1h, 2h, and 3h.

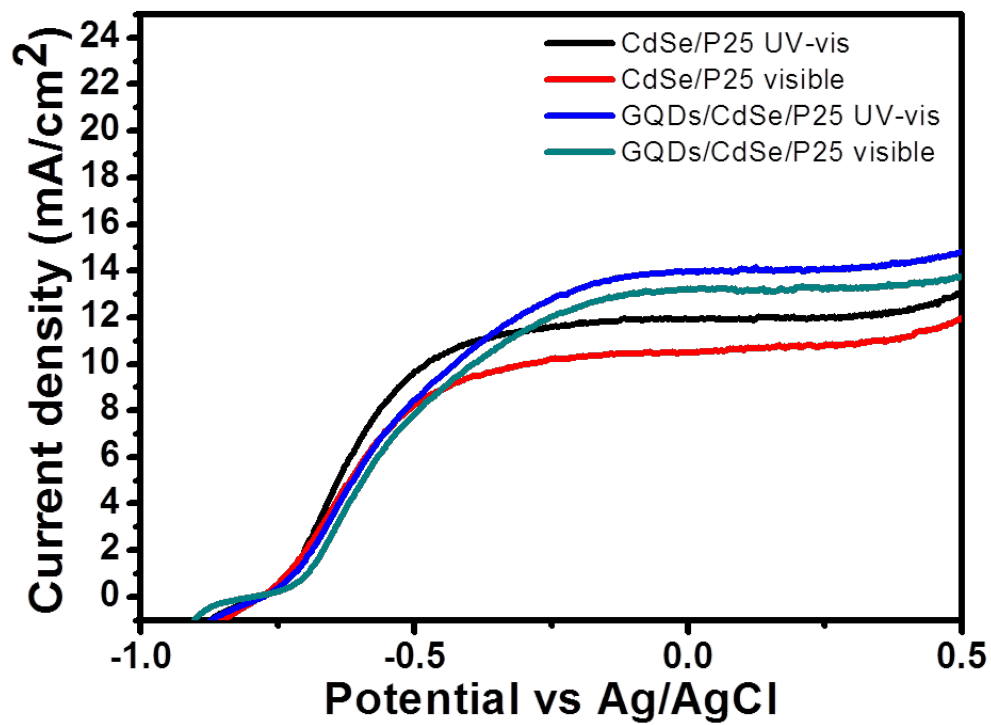


Figure 3.11 Photocurrent responses of CdSe/P25 and GQDs/CdSe/P25 under UV-visible and visible (>420 nm) light illumination.

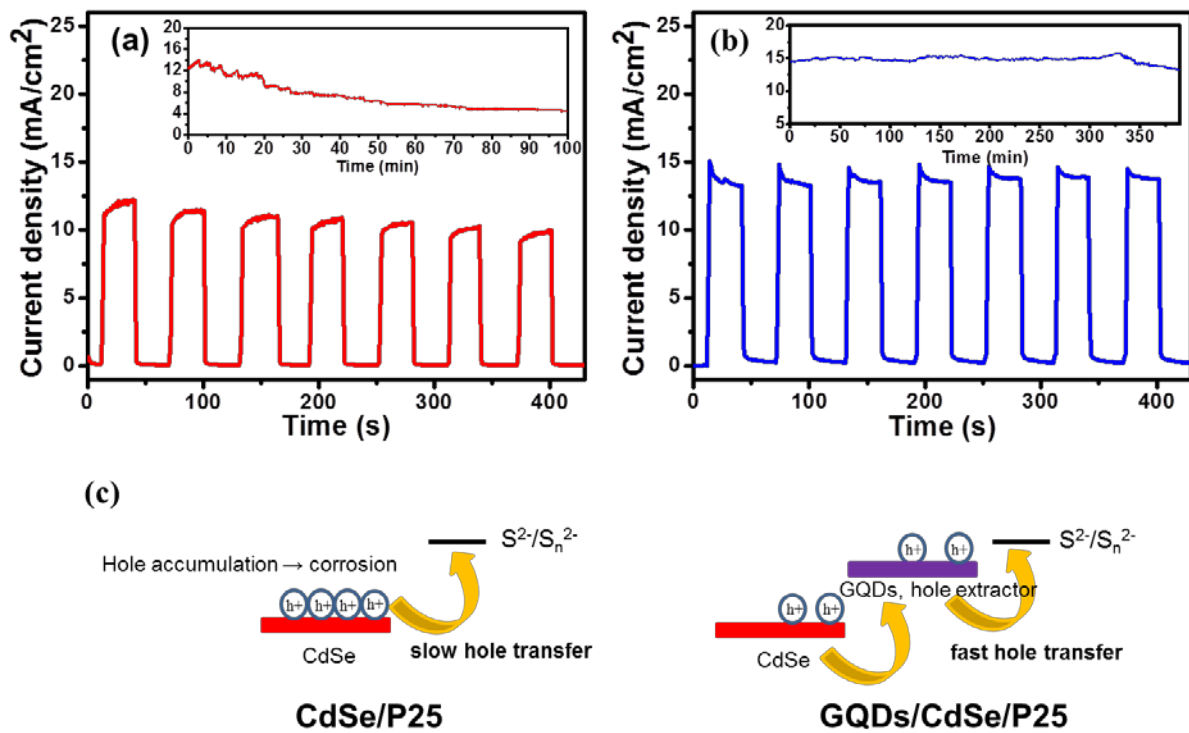
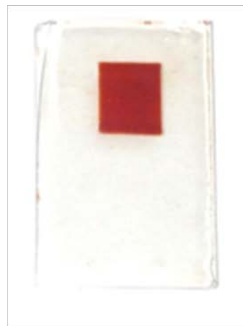


Figure 3.12 The J-T curve of (a) CdSe/P25 and (b) GQDs/CdSe/P25 at a bias of 0.3 V under light-chopping conditions. (c) Schematic diagram of the photoexcited hole transfer process.

(a) Before illumination



CdSe/P25



GQDs/CdSe/P25

(b) After illumination



CdSe/P25



GQDs/CdSe/P25

Figure 3.13 DC image of the photoanode (a) before and (b) after measuring.

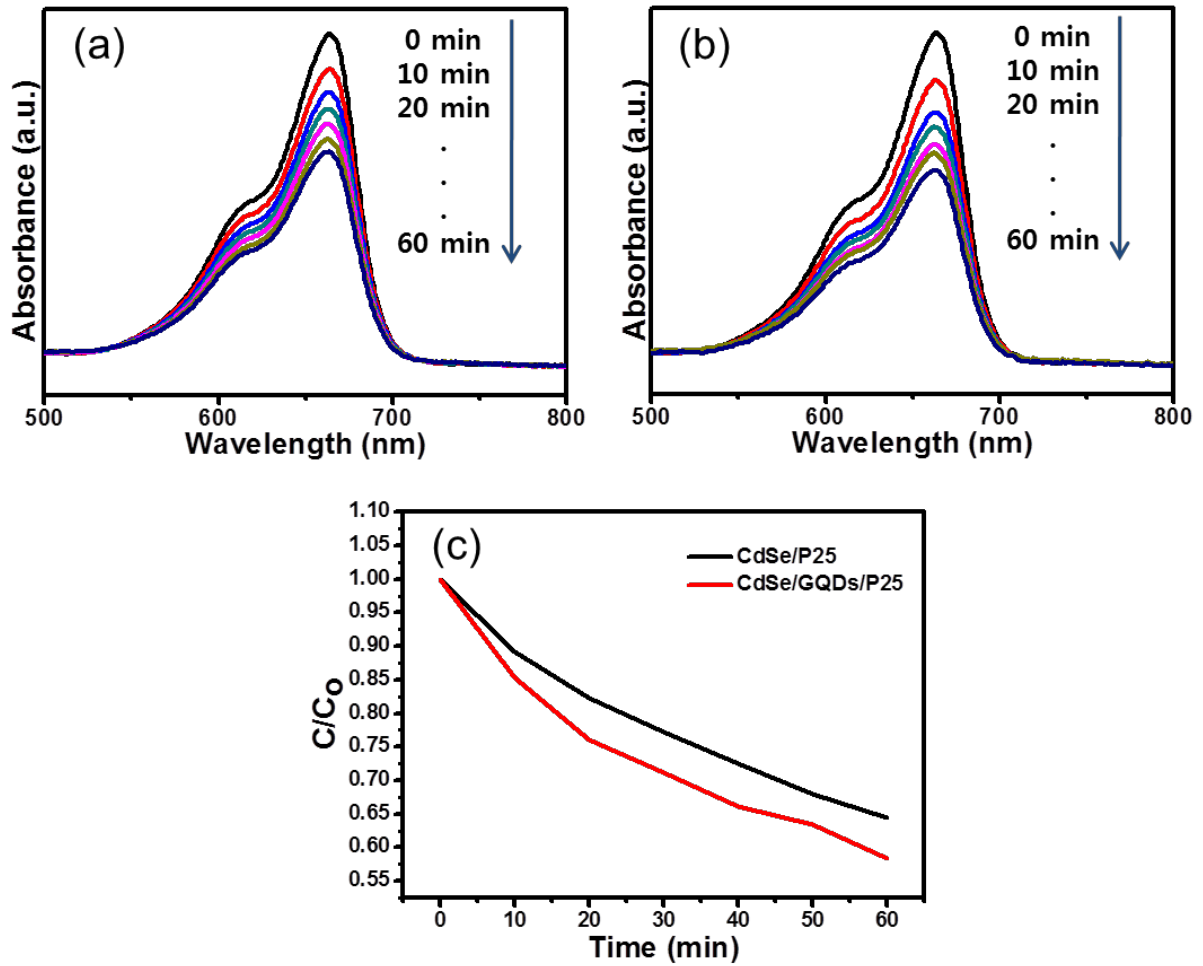


Figure 3.14 Time-dependent UV-vis absorbance of the photodegradation of methylene blue dye for (a) CdSe/P25 and (b) GQDs/CdSe/P25 electrodes. (c) Comparison of photocatalytic activity of two devices.

3.4 Conclusion

In summary, we have successfully fabricated a novel GQD supported CdSe-sensitized photoanode for visible light-working photoelectrochemical hydrogen generation. By modifying CdSe/TiO₂ with inexpensive GQDs, the photocurrent density was retained almost unchanged for 300 minutes' irradiation and the photocurrent density increased by 1.2 times relative to that without GQDs at 0.3 V vs Ag/AgCl. Fast interfacial charge transfer kinetics, confirmed by EIS and photoactivity measurements, clearly reveals that the GQDs help to release photogenerated holes accumulated on the surface of CdSe quantum dots, which in turn reduces hole-induced anodic corrosion of quantum dots. Our work suggests a straightforward way to develop efficient and durable quantum-dot-sensitized photoanodes for PEC hydrogen generation.

3.5 References

1. Ahn, H. J.; Kwak, M. J.; Lee, J. S.; Yoon, K. Y.; Jang, J. H., Nanoporous hematite structures to overcome short diffusion lengths in water splitting. *J. Mater. Chem. A* **2014**, *2*, 19999.
2. Yoon, K. Y.; Lee, J. S.; Kim, K.; Bak, C. H.; Kim, S. I.; Kim, J. B.; Jang, J. H., Hematite-Based Photoelectrochemical Water Splitting Supported by Inverse Opal Structures of Graphene. *ACS Appl. Mater. Interf.* **2014**, *6*, 22634.
3. Fujishima, A.; Honda, K., Electrochemical Photolysis of Water at a Semiconductor Electrode. *Nature* **1972**, *238*, 37.
4. Kim, K.; Thiagarajan, P.; Ahn, H. J.; Kim, S. I.; Jang, J. H., Optimization for Visible Light Photocatalytic Water Splitting: Gold-Coated and Surface-Textured TiO₂ Inverse Opal Nano-Networks. *Nanoscale* **2013**, *5*, 6254.
5. Park, J. H.; Kim, S.; Bard, A. J., Novel Carbon-Doped TiO₂ Nanotube Arrays with High Aspect Ratios for Efficient Solar Water Splitting. *Nano Lett.* **2006**, *6*, 24.
6. In, S.; Orlov, A.; Berg, R.; Garcia, F.; Pedrosa-Jimenez, S.; Tikhov, M. S.; Wright, D. S.; Lambert, R. M., Effective visible light-activated B-Doped and B,N-Codoped TiO₂ photocatalysts. *J. Am. Chem. Soc.* **2007**, *129*, 13790.
7. Liu, G.; Yin, L. C.; Wang, J. Q.; Niu, P.; Zhen, C.; Xie, Y. P.; Cheng, H. M., A Red Anatase TiO₂ Photocatalyst for Solar Energy Conversion. *Energy. Environ. Sci.* **2012**, *5*, 9603.
8. Xu, Z. H.; Yu, J. G., Visible-Light-Induced Photoelectrochemical Behaviors of Fe-Modified TiO₂ Nanotube Arrays. *Nanoscale* **2011**, *3*, 3138.
9. Lazar, M. A.; Daoud, W. A., Achieving Selectivity in TiO₂-Based Photocatalysis. *Rsc Adv.* **2013**, *3*, 4130.
10. Xiang, Q. J.; Yu, J. G.; Jaroniec, M., Synergetic Effect of MoS₂ and Graphene as Cocatalysts for Enhanced Photocatalytic H₂ Production Activity of TiO₂ Nanoparticles. *J. Am. Chem. Soc.* **2012**, *134*, 6575.
11. Leung, D. Y. C.; Fu, X. L.; Wang, C. F.; Ni, M.; Leung, M. K. H.; Wang, X. X.; Fu, X. Z., Hydrogen Production over Titania-Based Photocatalysts. *ChemSusChem* **2010**, *3*, 681.
12. Ahn, H. J.; Kim, M. J.; Kim, K.; Kwak, M. J.; Jang, J. H., Optimization of Quantum Dot-Sensitized Photoelectrode for Realization of Visible Light Hydrogen Generation. *Small* **2014**, *10*, 2325.
13. Li, G. S.; Zhang, D. Q.; Yu, J. C., A New Visible-Light Photocatalyst: CdS Quantum Dots Embedded Mesoporous TiO₂. *Environ. Sci. Technol.* **2009**, *43*, 7079.
14. Ratanatawanate, C.; Xiong, C. R.; Balkus, K. J., Fabrication of PbS quantum dot doped TiO₂ nanotubes. *ACS Nano* **2008**, *2*, 1682.
15. Chakrapani, V.; Baker, D.; Kamat, P. V., Understanding the Role of the Sulfide Redox

- Couple (S^{2-}/S_n^{2-}) in Quantum Dot-Sensitized Solar Cells. *J. Am. Chem. Soc.* **2011**, *133*, 9607.
16. Bang, J. H.; Kamat, P. V., Quantum Dot Sensitized Solar Cells. A Tale of Two Semiconductor Nanocrystals: CdSe and CdTe. *ACS Nano* **2009**, *3*, 1467.
 17. Seol, M.; Jang, J. W.; Cho, S.; Lee, J. S.; Yong, K., Highly Efficient and Stable Cadmium Chalcogenide Quantum Dot/ZnO Nanowires for Photoelectrochemical Hydrogen Generation. *Chem. Mater.* **2013**, *25*, 184.
 18. Sheng, W. J.; Sun, B.; Shi, T. L.; Tan, X. H.; Peng, Z. C.; Liao, G. L., Quantum Dot-Sensitized Hierarchical Micro/Nanowire Architecture for Photoelectrochemical Water Splitting. *ACS Nano* **2014**, *8*, 7163.
 19. Shen, J. H.; Zhu, Y. H.; Yang, X. L.; Li, C. Z., Graphene Quantum Dots: Emergent Nanolights for Bioimaging, Sensors, Catalysis and Photovoltaic Devices. *Chem. Commun.* **2012**, *48*, 3686.
 20. Schnez, S.; Molitor, F.; Stampfer, C.; Guttinger, J.; Shorubalko, I.; Ihn, T.; Ensslin, K., Observation of Excited States in a Graphene Quantum Dot. *Appl. Phys. Lett.* **2009**, *94*, 012107
 21. Peng, J.; Gao, W.; Gupta, B. K.; Liu, Z.; Romero-Aburto, R.; Ge, L. H.; Song, L.; Alemany, L. B.; Zhan, X. B.; Gao, G. H.; Vithayathil, S. A.; Kaiparettu, B. A.; Marti, A. A.; Hayashi, T.; Zhu, J. J.; Ajayan, P. M., Graphene Quantum Dots Derived from Carbon Fibers. *Nano Lett.* **2012**, *12*, 844.
 22. Dong, Y. Q.; Li, G. L.; Zhou, N. N.; Wang, R. X.; Chi, Y. W.; Chen, G. N., Graphene Quantum Dot as a Green and Facile Sensor for Free Chlorine in Drinking Water. *Anal. Chem.* **2012**, *84*, 8378.
 23. Son, D. I.; Kwon, B. W.; Park, D. H.; Seo, W. S.; Yi, Y.; Angadi, B.; Lee, C. L.; Choi, W. K., Emissive ZnO-Graphene Quantum Dots for White-Light-Emitting Diodes. *Nat. Nanotechnol.* **2012**, *7*, 465.
 24. Liu, Q.; Guo, B. D.; Rao, Z. Y.; Zhang, B. H.; Gong, J. R., Strong Two-Photon-Induced Fluorescence from Photostable, Biocompatible Nitrogen-Doped Graphene Quantum Dots for Cellular and Deep-Tissue Imaging. *Nano Lett.* **2013**, *13*, 2436.
 25. Beenken, W. J. D., Photo-Induced Charge Transfer in Fullerene-Oligothiophene Dyads - A Quantum-Chemical Study. *Chem. Phys.* **2009**, *357*, 144.
 26. Zerza, G.; Scharber, M. C.; Brabec, C. J.; Sariciftci, N. S.; Gomez, R.; Segura, J. L.; Martin, N.; Srdanov, V. I., Photoinduced Charge Transfer Between Tetracyano-Anthraquino-Dimethane Derivatives and Conjugated Polymers for Photovoltaics. *J. Phys. Chem. A* **2000**, *104*, 8315.
 27. Zhao, L.; Chen, X. F.; Wang, X. C.; Zhang, Y. J.; Wei, W.; Sun, Y. H.; Antonietti, M.; Titirici, M. M., One-Step Solvothermal Synthesis of a Carbon@TiO₂ Dyade Structure Effectively Promoting Visible-Light Photocatalysis. *Adv. Mater.* **2010**, *22*, 3317.
 28. Carlson, B.; Leschkies, K.; Aydil, E. S.; Zhu, X. Y., Valence Band Alignment at Cadmium

- Selenide Quantum Dot and Zinc Oxide (10(1)over-bar0) interfaces. *J. Phys. Chem. C* **2008**, *112*, 8419.
29. Higashi, M.; Domen, K.; Abe, R., Fabrication of an Efficient BaTaO₂N Photoanode Harvesting a Wide Range of Visible Light for Water Splitting. *J. Am. Chem. Soc.* **2013**, *135*, 10238.
30. Kim, J. K.; Park, M. J.; Kim, S. J.; Wang, D. H.; Cho, S. P.; Bae, S.; Park, J. H.; Hong, B. H., Balancing Light Absorptivity and Carrier Conductivity of Graphene Quantum Dots for High-Efficiency Bulk Heterojunction Solar Cells. *ACS Nano* **2013**, *7*, 7207.
31. Titirici, M. M.; Thomas, A.; Yu, S. H.; Muller, J. O.; Antonietti, M., A Direct Synthesis of Mesoporous Carbons with Bicontinuous Pore Morphology from Crude Plant Material by Hydrothermal Carbonization. *Chem. Mater.* **2007**, *19*, 4205.
32. Some, S.; Kim, Y.; Yoon, Y.; Yoo, H.; Lee, S.; Park, Y.; Lee, H., High-Quality Reduced Graphene Oxide by a Dual-Function Chemical Reduction and Healing Process. *Sci. Rep.* **2013**, *3*.
33. Zhang, M. L.; Jin, F.; Zheng, M. L.; Liu, J.; Zhao, Z. S.; Duan, X. M., High Efficiency Solar Cell Based on ZnO Nanowire Array Prepared by Different Growth Methods. *RSC Adv.* **2014**, *4*, 10462.
34. Kelkar, S.; Ballal, C.; Deshpande, A.; Warule, S.; Ogale, S., Quantum Dot CdS Coupled Cd₂SnO₄ Photoanode with High Photoelectrochemical Water Splitting Efficiency. *J. Mater. Chem. A* **2013**, *1*, 12426.
35. Jun, H.; Im, B.; Kim, J. Y.; Im, Y. O.; Jang, J. W.; Kim, E. S.; Kim, J. Y.; Kang, H. J.; Hong, S. J.; Lee, J. S., Photoelectrochemical Water Splitting Over Ordered Honeycomb Hematite Electrodes Stabilized by Alumina Shielding. *Energ. Environm. Sci.* **2012**, *5*, 6375.
36. Sanchez, C.; Sieber, K. D.; Somorjai, G. A., The Photoelectrochemistry of Niobium Doped Alpha-Fe₂O₃. *J. Electroanal. Chem.* **1988**, *252*, 269.
37. Lakshmi, S.; Renganathan, R.; Fujita, S., Study on Tio₂-Mediated Photocatalytic Degradation of Methylene-Blue. *J. Photoch. Photobio. A* **1995**, *88*, 163.

Acknowledgement

우선 석사 과정 동안 부족한 저에게 많은 기회를 주시고, 가르침을 주신 장지현 교수님께 진심으로 감사 드립니다. 또한 바쁘신 와중에도 논문 심사에 응해주신 주상훈 교수님과 서관용 교수님께도 감사의 말씀을 드립니다. UNIST에 와서 배워보지도 않은 분야의 연구를 시작하며 많이 힘들었지만 많은 조언과 도움을 주신 실험실 모든 분들께 진심으로 감사 드립니다. 같은 하늘아래 같은 공기를 마시며 만들었던 추억들 모두 소중히 간직하며 감사한 마음 잊지 않도록 하겠습니다. 이 정도 말했으면 제가 2년동안 UNIST에 와서 하루 동안 감사하다는 말을 가장 많이 한 것 같으니 더 이상 말하지 않아도 제가 얼마나 감사해 하는지 알거라 생각합니다.

마지막으로 잘 다니던 회사를 그만두고 공부하겠다고 했을 때 믿어주신 아버지, 어머니.. 남들 직장생활하고 집사고 결혼하고 할 시기에 집안의 장남이 아직도 공부 하겠다고 억지부리고 있는 거 같아 항상 죄송한 마음이지만 그래도 계속 믿어주시는 부모님께 늘 감사해 하고 있습니다. 그리고 내 동생 정용아 너도 드디어 철이 들었는지 어느 새 집보다 도서관에 있는 시간이 많아졌구나..평생 만나니처럼 살 줄 알았는데 역시 사람은 벼랑 끝에 서봐야 변하는 것 같다. 지금은 외롭고 힘든 시간이겠지만 힘내서 네가 원하는 목표를 달성했으면 싶다. 아 그리고 5천원짜리 커피 마실 거라고 부모님한테 용돈 달라고 그만하고 그냥 자판기 커피 마셔라. 형으로써 뭔가 도와줘야 하는데 그러지 못해 미안하다. 나중에 맛있는 거 사줄게

다시 한번 저의 석사생활을 무사히 마치게 해준 모든 분들께 진심으로 감사의 말씀을 드립니다.